

MECHANICAL PROPERTIES AND MICROSTRUCTURAL CHARACTERISTICS OF AN
Al-Mg ALLOY WITH BIMODAL GRAIN SIZE AT ROOM AND ELEVATED
TEMPERATURES

by

ANDREW C. MAGEE

LEILA LADANI, COMMITTEE CHAIR

BRIAN JORDON
GREGORY THOMPSON
MARK WEAVER
KEITH WOODBURY

A THESIS

Submitted in partial fulfillment of the requirements
for the degree of Master of Science
in the Department of Mechanical Engineering
in the Graduate School of
The University of Alabama

TUSCALOOSA, ALABAMA

2012

Copyright Andrew C. Magee 2012
ALL RIGHTS RESERVED

ABSTRACT

The strength of aluminum alloy 5083 has been shown to be significantly improved when it is engineered to have a bimodal grain size consisting of coarse grains (CGs) embedded in an ultrafine grained (UFG) matrix. This study investigates how a variety of parameters including strain rate, temperature, specimen thickness, CG ratio, and anisotropy affect the mechanical properties of this material when tested in uniaxial tension. The material is fabricated through cryomilling, cold isostatic pressing, and extrusion. A full factorial experiment is designed and implemented to test these effects on the material. Post-test examination of the specimens with optical and electron microscopes is conducted in order to gain a deeper understanding of the material's fracture behavior. While the material shows greatly improved strength compared to conventional Al-Mg alloys at room temperature, its strength rapidly decreases with rising temperature such that by 473 K, it was observed to be weaker than conventional Al 5083 at the same temperature. Dynamic recovery was observed in high temperature tests and the amount of recovery was found to depend on the material's CG ratio. Strain rate sensitivity was observed in the material at all temperatures. Significant differences were observed both in the material's properties and its fracture surface when the specimens were loaded parallel or perpendicular to the extrusion direction. A constitutive model based on Joshi's model of plasticity was developed to describe the material's room temperature behavior.

LIST OF ABBREVIATIONS AND SYMBOLS

Abbreviations:

CG	Coarse grained
CIP	Cold isostatic pressing
DSA	Dynamic strain aging
EBS	Electron backscatter diffraction
EDM	Electric discharge machining
FEA	Finite element analysis
HAZ	Heat affected zone
HIP	Hot isostatic pressing
NC	Nanocrystalline
PCA	Process control agent
PPB	Prior particle boundary
SEM	Scanning electron microscope
UFG	Ultrafine grained
UTS	Ultimate tensile stress

Symbols:

A_c	Projected contact area
d	Grain size
E	Elastic modulus
E_r	Reduced modulus
k	Hall-Petch material constant
m	Strain rate sensitivity exponent
p	Probability of null hypothesis being true as determined by ANOVA
R_{att}	Attenuating resistance
r_{ext}	Strain gauge recorder range extension factor
R_G	Strain gauge resistance
R_L	Lead wire resistance
S	Unloading stiffness
T	Temperature
ε	Strain
$\dot{\varepsilon}$	Strain rate
ε_c	Characteristic strain
ε_j	Starting strain of Joshi's model
ε_p	Plastic strain
ε_u	Ultimate strain
ν	Poisson's ratio
σ	Stress

σ_f	Flow stress
σ_j	Starting stress of Joshi's model
σ_s	Saturation stress
σ_y	Yield stress (0.2% offset method unless otherwise noted)

ACKNOWLEDGMENTS

Firstly, I would like to thank my adviser Dr. Leila Ladani for all of her help, support, and guidance over the course of my degree. I would also like to thank my thesis committee, Dr. Brian Jordon, Dr. Gregory Thompson, Dr. Mark Weaver, and Dr. Keith Woodbury for their support.

Thanks to everyone in my research group, Evan Harvey, Ousama Abdelhadi, and Allison Copus for their help along the way. Thanks also to Brittney Ellison for her invaluable assistance with my experimental work.

Thanks to Dr. Mark Weaver and Dr. Mark Barkey for getting me started at the very beginning by showing me the basics of how to attach a strain gauge and conduct a tensile test.

I would like to thank the staff of the Central Analytical Facility here at UA for their unfailing help and use of their resources. I would also like to acknowledge the National Science Foundation for supporting my work. This material is based upon work supported by the NSF under grant number 1053434.

Finally, I would like to thank my family for their support and encouragement.

TABLE OF CONTENTS

ABSTRACT.....	ii
LIST OF ABBREVIATIONS AND SYMBOLS	iii
ACKNOWLEDGMENTS	vi
LIST OF TABLES	ix
LIST OF FIGURES	x
CHAPTER 1 INTRODUCTION.....	1
1.1 Background	1
1.2 Motivation and Objectives	3
CHAPTER 2 LITERATURE REVIEW.....	5
2.1 Fabrication of a Bimodal Al-Mg Alloy.....	5
2.2 Known Effects.....	8
CHAPTER 3 EXPERIMENTAL PROCEDURES	13
3.1 Material Fabrication	13
3.2 Mechanical Testing	13
3.3 Microstructural Analysis	17
CHAPTER 4 RESULTS AND DISCUSSION	18

4.1	CG Ratio Effects	20
4.2	Anisotropy Effects.....	23
4.3	Strain Rate Effects.....	27
4.4	Thickness Effects	30
4.5	Temperature Effects	34
CHAPTER 5 CONSTITUTIVE MODEL.....		46
CHAPTER 6 CONCLUSIONS.....		50
6.1	Effects of Test Parameters.....	50
6.2	Contribution	52
6.3	Future Work	52
APPENDIX A SPECIMEN AND TEST FIXTURE DESIGN		53
APPENDIX B EXTENDING THE RANGE OF THE P3 STRAIN GAUGE RECORDER		56
REFERENCES		58

LIST OF TABLES

Table 1 Percent Element Composition of Al-5083.....	1
Table 2 Previously Reported Properties of UFG and Bimodal Al Alloys	8
Table 3 Experiment Plan.....	16
Table 4 ANOVA Results for Main Effects.....	20
Table 5 Effect of Temperature on Ductility.....	44
Table 6 Average Model Constants.....	48
Table 7 Reduced Table of Model Constants.....	49

LIST OF FIGURES

Figure 1. Tensile curves of bimodal Al-Mg alloys with different CG ratios [16].	3
Figure 2. EBSD images of the finished material. Arrows indicate extrusion direction.	7
Figure 3. Test specimen. Dimensions in mm.	14
Figure 4. Specimen with strain gauge attached. Dime included for scale.	14
Figure 5. Test Resources 800LE load frame and thermal chamber. P3 recorder is visible in the lower left.	15
Figure 6. (a) Elastic modulus, (b) 0.2% offset line, (c) yield stress, (d) UTS, (e) ultimate strain. Curve is from a 30% CG ratio, longitudinal, 1 mm thick specimen tested at 293 K and 10^{-5} s^{-1} .	19
Figure 7. Effect of CG ratio on strength in the longitudinal direction.	21
Figure 8. Effect of CG ratio on ductility in the longitudinal direction.	21
Figure 9. CG region in the UFG matrix on the fracture surface of a 10% CG material.	22
Figure 10. (a-d) FEA simulation of crack propagation. Purple areas are CGs, blue areas are UFGs. Red/green elements have failed. [48]	23
Figure 11. Effect of anisotropy and CG ratio on strength.	24
Figure 12. Effect of anisotropy and CG ratio on ductility.	24
Figure 13. Tests at 20% CG ratio showing reduction in plasticity.	25
Figure 14. Optical micrographs of failure surfaces in profile of (a) longitudinal and (b) transverse specimens. The side of the longitudinal specimen shown here has been prepared for strain gauge application, while the transverse specimen shows the original EDM surface texture.	26

Figure 15. Scanning electron micrographs of fracture surfaces in (a) longitudinal and (b) transverse directions.....	26
Figure 16. Effect of strain rate on strength.	27
Figure 17: Effect of strain rate on ductility.....	28
Figure 18. Enlarged section of a stress-strain curve from a test on a 0.5 mm longitudinal specimen at $1\text{E-}5 \text{ s}^{-1}$ showing serrations.....	29
Figure 19. Effect of specimen thickness on elastic modulus.....	30
Figure 20. Load-depth curves from nanoindentation tests conducted on this material in [52]. ...	31
Figure 21. SEM image of an indent in this material presented in [52].....	32
Figure 22. SEM images of fracture surfaces of (a) 0.5 mm and (b) 1 mm specimens in the longitudinal direction.	33
Figure 23. EBSD images of the microstructure in the transverse direction of specimens tested at 293 and 473 K.....	34
Figure 24. Histogram of grain size.	35
Figure 25. Effect of temperature on 10% CG material tested in the longitudinal direction at 10^{-5} s^{-1}	36
Figure 26. Enlarged view of the yield region of representative tests at 10^{-5} s^{-1} at 473 K at various CG ratios.	36
Figure 27. Effect of temperature on yield stress in the longitudinal direction. 5083-O data from [30].....	38
Figure 28. Effect of temperature on ultimate stress in the longitudinal direction. 5083-O data from [30].....	38
Figure 29. Longitudinal fracture surfaces from tests at different temperatures.....	40

Figure 30. Interaction of strain rate and temperature effects on yield strength.	41
Figure 31. Interaction of strain rate and temperature effects on ultimate strength.	41
Figure 32. Strain rate sensitivity exponent as a function of temperature.....	42
Figure 33. Effects of temperature and anisotropy on yield strength.....	43
Figure 34. Effects of temperature and anisotropy on ultimate strength.....	44
Figure 35. Fracture surfaces of (a) longitudinal and (b) transverse specimens.	45
Figure 36. Model fit to the experimental data from a 30% longitudinal 1 mm specimen tested at 10^{-5} s^{-1}	48
Figure 37. (left, middle) Old specimen designs showing unwanted failure locations. (right) Final specimen design with an acceptable failure location.....	54
Figure 38. Tensile grips.	54
Figure 39. Placement of attenuating resistors in a quarter-bridge configuration.....	57

CHAPTER 1

INTRODUCTION

1.1 Background

Nanocrystalline (NC) and ultrafine grain (UFG) materials have recently drawn much attention due to their drastically improved mechanical properties. This improvement is dictated to some extent by the Hall-Petch relationship. This relationship, shown in Equation 1, states that as the grain size, d , of a material decreases, its yield strength, σ_y , increases with σ_o and k being material constants [1].

$$\sigma_y = \sigma_o + \frac{k}{\sqrt{d}} \quad (\text{Eq. 1})$$

It should be noted that below a critical grain size, around 10 nm, further reduction in size weakens the material, a phenomenon known as the inverse Hall-Petch Effect, which is generally attributed to the increasingly important role of grain boundaries as grain size is refined beyond 10 nm [2].

One material that has been produced in UFG form is aluminum alloy 5083 for which the element composition is provided in Table 1.

Table 1
Percent Element Composition of Al-5083

Al	Si	Fe	Cu	Mn	Mg	Cr	Zn	Ti
92.55 - 94.25	0.4	0.4	0.1	0.4 - 1.0	4.0 - 4.9	0.05 - 0.25	0.25	0.15

Aluminum alloys are often favored for their light weight, but their low strength limits their usefulness in design. To combat this shortcoming, NC Al 5083 has been produced by cryomilling (low temperature mechanical milling) -325 mesh gas atomized powder to reduce grain size. The NC powder is then consolidated by a process such as hot or cold isostatic pressing (HIP or CIP). To break up prior particle boundaries (PPBs) remaining from the primary consolidation step, the material is usually subjected to further working such as extrusion or quasi-isostatic forging, after which the bulk consolidates are UFG in nature. Cryomilling and consolidation of UFG Al 5083 have been discussed extensively in the literature and are treated with greater depth in Section 2.1 [3-7]. From the aforementioned references, research has shown that secondary consolidation has a strong influence on the properties of UFG Al 5083 generated from cryomilled precursor powders. Strain rate, temperature, and the method of imparting deformation – forging, extrusion, and/or rolling – all play a role in determining the final microstructure and, hence, the strength and ductility of the consolidated material.

Regardless of processing path, UFG aluminum alloys produced by cryomilling have been found to have greatly improved strength compared to conventional aluminum alloys [8-10]. Unfortunately, the increased strength is accompanied by a decrease in ductility, limiting the applications of this material. Engineering a microstructure with multiple length scales has been proposed as a strategy to enhance the plasticity of nanostructured materials which otherwise lack adequate dislocation activity, and therefore exhibit low ductility. To that effect, various research groups have implemented this concept by promoting the formation of so called bimodal microstructures (e.g., consisting of a mixture of UFGs and CGs) which exhibit more balanced combinations of strength and ductility, shown in Figure 1 [11-16]. The resulting microstructure consists of both coarse grains with a grain size of a few microns and ultrafine grains with a size

of about 100-200 nm. The addition of the CGs returns some of the ductility to the material, at the cost of a small reduction in strength.

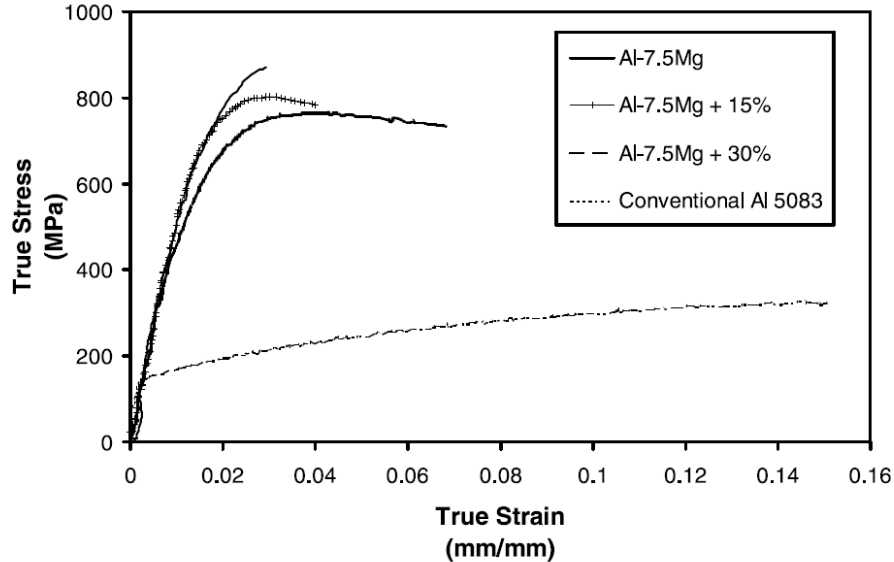


Figure 1. Tensile curves of bimodal Al-Mg alloys with different CG ratios [16].

While the means of producing this material and its basic properties are reasonably well understood, there is less knowledge about how this material responds to changes in its environment or to the demands of different design applications. Discussed in Section 2.2, there is evidence that a variety of factors such as strain rate, temperature, specimen thickness, anisotropy, and CG ratio can influence the properties of this material.

1.2 Motivation and Objectives

In order for this material to be more widely used in design applications, a better understanding of its material properties and how they are affected by the specific conditions of its application must be gained. The objective of this study is to understand mechanical behavior of a bimodal grain size Al alloy under different conditions. To this end, the material's behavior is evaluated in uniaxial tensile tests while several test parameters such as CG ratio, strain rate,

specimen thickness, anisotropy, and temperature are varied. A full factorial experiment on these factors is designed and executed.

In order to understand the microstructure of the material and its mechanisms of failure under the different conditions, a variety of pre-test and post-test microscopic analyses have been employed. The fracture surfaces are examined with an optical microscope and a scanning electron microscope (SEM) to study the mechanisms of deformation and failure. Additionally, electron backscatter diffraction (EBSD) images have been obtained in order to study the grain structure of the material before and after tests. Furthermore, constitutive models are generated in an attempt to describe and predict the material's behavior under different conditions. This model is useful for future finite element simulations. In all, it is expected that this work will provide a starting point for the complete characterization of this material so that its unique properties may be fully realized in design applications.

CHAPTER 2

LITERATURE REVIEW

2.1 Fabrication of a Bimodal Al-Mg Alloy

The general process of creating a bimodal alloy is fairly well understood. First the grain size of some parent material must be reduced, usually through a process known as cryomilling, to create a powder with a UFG grain size. Then the powder is mixed with unmilled powder to create a bimodal microstructure. The mixture is degassed to remove impurities then consolidated. Finally, the material is subjected to some sort of working process to break up PPBs and improve the properties of the final material.

As discussed in Chapter 1, the strength of this material lies in its small grain size. One technique used to reduce the grain size of a material is known as cryomilling, which is the method employed to produce the material used in this study. In the cryomilling process, a barrel is loaded with the metal powder and the milling medium, typically stainless steel balls. A process control agent (PCA) such as methanol, stearic acid, or paraffin is usually added to the mix to prevent the milled powder from becoming welded to the balls or recombining into larger particles [10]. As the name suggests, cryomilling takes place at very low temperature, which also helps prevent recombination of the particles. To achieve these temperatures, liquid nitrogen is circulated through the mixture and replenished as it evaporates. As the material is agitated, the milling medium and powder collide and the powder is broken up into smaller particles.

In addition to the Hall-Petch grain size strengthening, the material has also been observed to be strengthened through Orowan mechanisms resulting from the presence of dispersoids in the material [17]. As may be expected, many of these are compounds of elements Al, Mg, and O [18]. However, it is interesting to note the presence of some N-Al compounds contributing to the strengthening. The N in these compounds was introduced from the cryomilling process, illustrating another and somewhat unintentional pathway for the process to contribute to the material's strengthening [19].

After the cryomilling run is completed, the remaining liquid nitrogen is allowed to evaporate and the milled powder is mixed with the appropriate amount of unmilled powder to create the desired CG volume ratio. The mixed powder is then hot vacuum degassed to remove the PCA and other contaminants resulting from the cryomilling process. The powder is placed under a vacuum and heated to a prescribed temperature and held there for several hours. Naturally, the elevated temperature results in some undesired grain growth. However, this step is necessary in order to maximize the density of the billet after consolidation, especially if CIP will be employed [20].

The choice of consolidation method can have large impact on the properties of the final material. The two most common methods are CIP and HIP, although other methods such as quasi-isostatic forging or spark plasma sintering can be implemented [21-23]. In CIP and HIP, the powder is subjected to high pressure and, in the case of HIP, temperature to consolidate the powder into a cohesive unit. While higher densities can be obtained through HIP, it does cause more undesired grain growth [20]. Therefore, CIP, which is done at room temperature but requires a higher pressure, is sometimes preferred for the consolidation procedure. Additionally, CIP is more cost and time-effective than HIP when producing the material [11].

Regardless of whether CIP or HIP was chosen, the material now contains PPBs which adversely affect its properties. To remove them, some method of plastic deformation such as rolling, forging, or extrusion must be utilized. This step also serves to remove some of the remaining porosities in the material and bring it to its final density [24].

The material is now ready to be shaped into its final form. As shown in Figure 2, it now consists of CG bands embedded in a UFG matrix. The material shown in Figure 2 has been consolidated by CIP and extruded. Note the directionality of the microstructure imparted by the extrusion process. As may be expected, this property of the material's microstructure has a large impact on its properties and will be explored in-depth below.

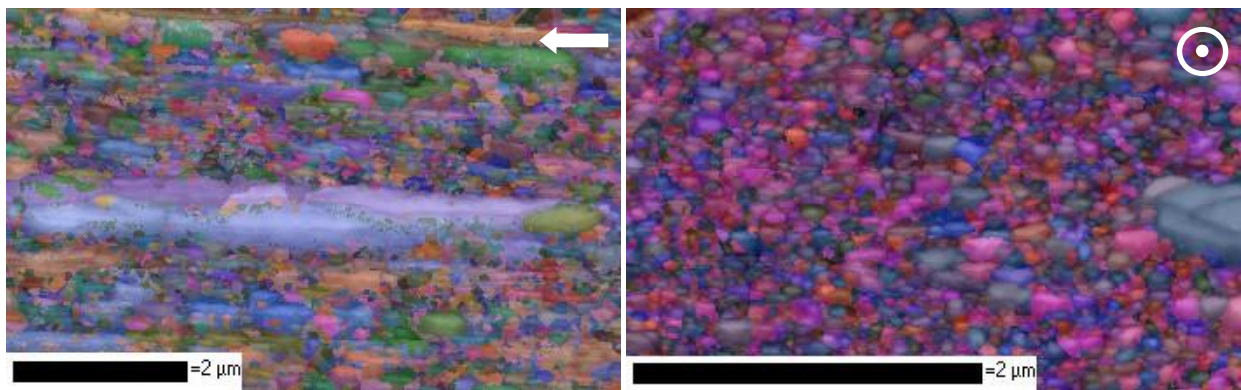


Figure 2. EBSD images of the finished material. Arrows indicate extrusion direction.

The bimodal microstructure of this material allows both the CG and UFG regions to share a load applied to the material and enables each region to exhibit its strong points. Initially, the CGs bear the load but their deformation is constrained by the UFGs. As loading continues, the CGs transfer the load to the UFGs through the activation of slip systems [25]. Each region also has its own dominant deformation mechanisms. In the CGs deformation was found to occur through dislocation slip, while twinning was observed in the UFGs [26].

2.2 Known Effects

It has been well established by a variety of research groups that UFG and bimodal Al alloys exhibit improved strength compared to conventional Al 5083, shown in Table 2. The penalty of this strengthening, reduction in ductility, as well as how to combat this problem is also understood. The uncertainty in using this material in design applications lies in its less well known responses to the specific conditions of an application.

Table 2
Previously Reported Properties of UFG and Bimodal Al Alloys

Source	Cons. Method	CG Size [μm]	UFG Size [nm]	Test Type	CG Ratio [%]	E [GPa]	σ_y [MPa]	Ultimate Stress [MPa]	Elongation [%]
[11]	CIP	4.0	247	T	50	--	270	--	7
[13]	CIP	1	200	C&T	0	69	700	780	1.5
					15	69	650	770	1.8
					30	65	500	650	2.1
					50	--	400	570	2.2
[16]	HIP	0.6-1.0	100-300	T	0	--	641	847	1.4
					15	--	630	778	2.4
					30	--	554	734	5.4
[27]	HIP	5	120	C	10	--	600-640	--	--
[28]	CIP	0	300	C&T	0	--	--	800-945	8
[29]	HIP	2.7-3.5	120-338	C&T	10	--	575-612	--	--
[30]	--	--	--	T	100	71	145	290	22

C: compression, T: tension

There has been some study on the different effects acting on bimodal Al 5083, but it is by no means complete and, in areas such as the effects of strain rate discussed below, there is some disagreement. In addition, differences in the conditions of the experiments described below leave room for further examination of the effects. For example, there has been much work on the compressive properties of this material. However, compression-tension asymmetry has been observed in this material [10,29] as well as in similar materials such as a cryomilled Al-10Ti-2Cu alloy [31]. Therefore, compression tests may not be sufficient to adequately describe the material's behavior when loaded in tension. Also, as described in Section 2.1, the process

parameters used during the creation of the material, notably CIP versus HIP, also affect the material's properties [9]. Thus, in order to provide fundamental insight into the behavior of these bimodal materials, additional mechanical behavior studies are required.

At the most basic level, the CG ratio used to produce the material affects its properties; this is indeed the reason why the CGs are included. As may be expected, as the CG ratio rises the material behaves more like a conventional Al alloy (low strength, high ductility) and less like a UFG alloy (high strength, low ductility). Thus, for a given application and its attendant strength and ductility requirements, there exists an optimal CG ratio. In their work, Han et al. [13], attribute the enhanced ductility to the crack bridging effect of adding CG powder to the material, while high strength is retained from the UFG regions.

Another effect, perhaps the most extensively examined effect acting on the material, is the effect of strain rate. However, conclusions on this effect seem to have been drawn exclusively from compression tests of the material. Two studies, conducted on bimodal Al 5083, have examined the strain rate effect in compression tests between 10^{-4} and 10^{-1} s^{-1} [27,29]. In one (Fan et al., 2006), tensile tests were also conducted, but the results of these tests in relation to the strain rate effect are not presented. The conclusions of these studies are that as strain rate is increased, this material's strength decreases and ductility increases.

Others have studied the strain rate effect in UFG-only Al. Han et al. varied the tensile strain rate between $4\text{E-}4$ and $4\text{E-}2 \text{ s}^{-1}$, and did not observe a significant strain rate effect [32]. A different study by Han et al. again found a small increase in ultimate strength of the material at lower strain rates but, contrary to the studies mentioned above, noted a decrease in ductility as strain rate was increased [33]. Strain rate jump experiments conducted by Hayes et al. on nanocrystalline pure Al also showed little strain rate sensitivity [34].

Another property of bimodal Al 5083 that has had some study devoted to it is the anisotropy derived from the extrusion process. Han et al. studied the differences in longitudinal and transverse samples in compression tests of the material [13]. They observed a significant decrease in strength and ductility in the transverse specimens when compared to the longitudinal specimens. This sort of anisotropic effect is common in extruded materials.

Size is another factor that has been shown to produce significant effects on mechanical behavior [35-38]. There are several different manifestations of the size effect that may serve to either strengthen or weaken a material. The most obvious size effect in this material is its increased strength due to the reduction in grain size. This “grain size effect” is discussed in Section 1.1. Other size effects occur as the dimensions of a specimen become comparable to the dimensions of a single grain and thus the specimen may have only a few grains across its cross-section. A consequence of this is that the properties and orientations of individual grains become more significant in the behavior of the material [35]. This effect has been noted to decrease the strength of specimens as they become smaller [35-37]. EBSD analysis of the material used in this study has shown that the UFGs are about 100 nm (Figure 2) and that even the large grains of this material are much smaller than the size of the specimen. Therefore, this effect is not expected to contribute much to the material’s behavior unless there is an analogous effect due to the coarse grained bands which can be up to 20 μm wide and 240 μm long, depending on the initial CG ratio of the powder [15].

Another type of size effect occurs due to the unavoidable surface damage resulting from machining. In large specimens, the properties of the damaged region are not significant because this region is vanishingly small compared to the total volume of the specimen. However, the damaged areas make up an increasingly significant portion of the total material volume as the

size of the specimen is reduced. A study on laser sectioned pure Al showed that narrower specimens were stronger due to the laser cutting process, which resulted in a hardened area near the cut surfaces [38]. Similarly, an affected area has been noted in materials sectioned by electric discharge machining (EDM) [39-40], which is how the specimens used in this study are produced. This affected area, which consists of a heat affected zone (HAZ) and a recast layer, is typically less than 30 μm thick. Some reports indicate that HAZ's may not even occur in Al sectioned by EDM [41].

While the general effects of increased temperature (e.g., reduced strength and increased ductility) are straightforward, these effects can be complicated in a variety of ways making the ultimate effect of temperature not entirely predictable. For example, the failure strain of some nanostructured Al-Mg alloys has been noted to have a non-monotonic dependence on temperature, meaning that not even the general maxim of increased ductility with increased temperature can be taken as absolute [42]. Furthermore, temperature may affect not only the material itself, but also interact with the other effects acting on the material, making the problem of predicting the material's properties in a given environment more complicated.

As mentioned previously, this aluminum alloy has been observed to exhibit slight negative strain rate sensitivity (a decrease in strength at higher strain rates) at room temperature. The effects of temperature on strain rate sensitivity are difficult to predict. The room temperature sensitivity has been explained by dynamic strain aging (DSA), where solute atoms diffuse to block the movement of dislocations. At higher strain rates the atoms cannot move fast enough to effectively block the dislocations, leading to negative strain rate sensitivity.

The effect of temperature on the strain rate sensitivity exponent of the pure UFG form of this material has been examined through compression tests [43]. The exponent was small and

negative at room temperature and increased to 0.15-0.28 with increasing temperature. The increase in the exponent is attributed to diminished work hardening at elevated temperatures. Additionally, the effects of loading at dynamic rates have been studied and suggest a change in dominance of thermal softening mechanisms with strain rate [44]. At higher rates, the activation of effects such as DSA and creep are limited making thermally activated dislocation motion the primary method of thermal softening.

At least when consolidated by high temperature methods such as HIP or quasi-isostatic forging, the UFG microstructure of this material is very stable [44-45]. No significant grain growth has been noted after annealing times of as long as 996 hours at 573 K [46]. It is possible that the heat added during the HIP process allows the material to recover from cryomilling. If the powder is consolidated at relatively low temperatures such as by CIP, it may be that this recovery is not possible and that the method of consolidation affects the material's response to temperature.

With these effects in mind, a full factorial experiment was designed to test the effects of strain rate, CG ratio, temperature, specimen thickness, and anisotropy on a cryomilled bimodal Al 5083 alloy consolidated by CIP and extruded. This experiment will test these effects on the material's mechanical properties through uniaxial tensile tests.

CHAPTER 3

EXPERIMENTAL PROCEDURES

3.1 Material Fabrication

UFG Al powder was synthesized by cryomilling Al-5083 powder in liquid nitrogen (~77 K) for 8 hours. The UFG powder was V-blended (a low-shear method of mixing powders) with the unmilled powder to create 10, 20, and 30% CG mixtures. The mixtures were then hot vacuum degassed at 723 K for 8 hours in order to remove contaminants such as H, C, and O resulting from cryomilling. The powder was then consolidated by CIP at room temperature at a pressure of approximately 300 MPa for five minutes. To break up PPBs, the material was then extruded. The billet was placed in a furnace at 797 K for 30 minutes prior to extrusion. The extrusion process, with a ratio of about 6:1, was performed in a high-strain rate Dynapak extrusion press which utilizes gas pressure (rather than hydraulics) to force the billet through the die in a matter of milliseconds, resulting in a rod about 2 cm in diameter.

3.2 Mechanical Testing

Specimens were sectioned via EDM from the material both in the direction of extrusion (longitudinal) and across the face of the extruded bar (transverse). The shape and dimensions of the specimen are shown in Figure 3. Specimens were sectioned to two thicknesses: 1 mm and 0.5 mm. The specimen's dimensions were constrained by the dimensions of the bulk material from which they were cut, which was only about 2 cm in diameter. Thus, these specimens are much

smaller than the specimens traditionally used in tensile tests. There are no ASTM standards for specimens of this size, so the constraints of the bulk material were used to determine the specimen dimensions. More information on the design of the specimen can be found in Appendix A.

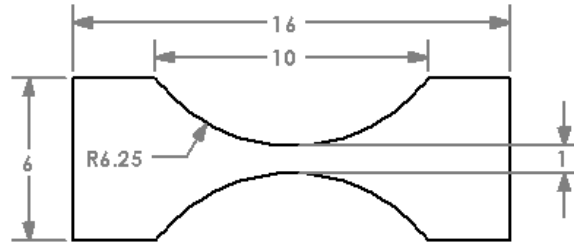


Figure 3. Test specimen. Dimensions in mm.

Due to the small size of the specimens, it is crucial to measure the strain directly within the gauge length to avoid errors caused by crosshead and load cell compliance and the fixture tolerances. Therefore, strain gauges were attached to the specimens per the manufacturer's instructions using Vishay M-Bond 200 adhesive for the room temperature tests and M-Bond AE-10 adhesive for the high temperature tests. As shown in Figure 4, the gauge's grid is only about 0.5 mm by 0.5 mm, and it can measure up to 10% strain.

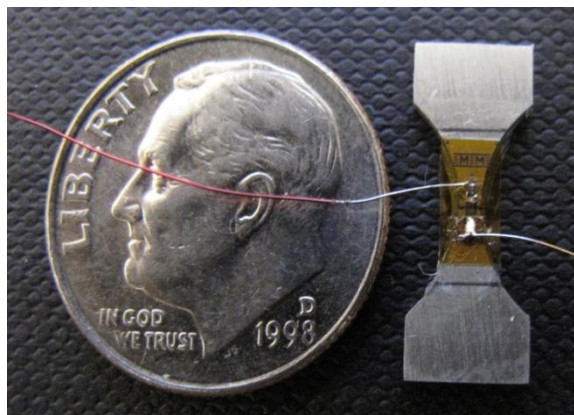


Figure 4. Specimen with strain gauge attached. Dime included for scale.

Tests were conducted on a Test Resources 800LE load frame (Figure 5) under displacement control with a 2000 lb (~9 kN) load cell. This frame/load cell combination provides a displacement resolution of 0.5 μm and a force accuracy of about $\pm 0.2\%$. Strain data was captured using a Vishay P3 strain gauge recorder. The range of this instrument was extended as described in Appendix B in order to be able to capture a larger part of the plastic region. At temperatures above room temperature, the specimens were allowed to soak at the test temperature for 30-45 minutes until thermal expansion of the testing apparatus had become negligible.



Figure 5. Test Resources 800LE load frame and thermal chamber. P3 recorder is visible in the lower left.

The full factorial experiment was designed to test three instances of the material, each with a different CG ratio, at three temperatures, two material orientations, two thicknesses, and two strain rates. As shown in Table 3, this resulted in 72 different combinations of conditions. At

least three trials were performed for each combination of conditions, resulting in over 200 individual tests.

Table 3
 Experiment Plan
 (repeated for 10%, 20%, and 30% CG ratios)

Run	Temperature [K]	Orientation	Thickness [mm]	Strain Rate [s ⁻¹]
1	293	Longitudinal	1	1.00E-04
2				1.00E-05
3			0.5	1.00E-04
4				1.00E-05
5		Transverse	1	1.00E-04
6				1.00E-05
7			0.5	1.00E-04
8				1.00E-05
9	383	Longitudinal	1	1.00E-04
10				1.00E-05
11			0.5	1.00E-04
12				1.00E-05
13		Transverse	1	1.00E-04
14				1.00E-05
15			0.5	1.00E-04
16				1.00E-05
17	473	Longitudinal	1	1.00E-04
18				1.00E-05
19			0.5	1.00E-04
20				1.00E-05
21		Transverse	1	1.00E-04
22				1.00E-05
23			0.5	1.00E-04
24				1.00E-05

The strain rates were selected based on the limitations in the recording rate of the P3 recorder, which could not record fast enough to generate a meaningful set of data at higher strain rates. Likewise, the temperatures were determined by the strain gauges operational limits. It should be noted that 473 K is a significant portion of the 863 K melting point of Al 5083 [30] so

that in spite of the limitations of the strain gauge, an accurate portrayal of the material's behavior at elevated temperatures was captured.

3.3 Microstructural Analysis

Post-test analysis of the fracture surfaces was conducted using optical microscopy and scanning electron microscopy (SEM) on a JEOL-7000 FE SEM. The SEM was also used to conduct electron backscatter diffraction (EBSD) analysis of the material's grain structure both pre- and post-test.

To obtain high quality EBSD images, proper preparation of the sample's surface is very important. Samples were mounted in a conductive resin and allowed to set overnight. After it had set, the resin was ground away on a polishing wheel to expose the specimen. The specimens were then roughly polished by 600 and 800 grit silicon carbide paper in succession. To remove the scratches left over from the grinding process, the samples were polished using 1 μm aluminum oxide polishing compound. The specimens' surface finish was periodically inspected under an optical microscope to determine when they had been sufficiently polished. Finally, the specimens were placed in a vibratory polisher with 0.05 μm colloidal silica for 4 hours.

The specimens were cleaned by putting them in the vibratory polisher with distilled water for 30 seconds. They were then placed in an ultrasonic cleaner for 20 minutes and rinsed with acetone. To resolve charging issues during the EBSD scan, the surface of the resin puck enclosing the specimens was painted with conductive carbon paint.

CHAPTER 4

RESULTS AND DISCUSSION

The following sections will examine the parameters' effects on the material's properties. The properties examined here elastic modulus, yield strength, ultimate tensile stress (UTS), and ultimate strain. These points are depicted on a sample stress-strain curve in Figure 6. The elastic modulus, E , is the slope of the initial linear elastic region of the stress-strain curve. It is determined by taking the slope of a line fit to this region of the curve. The yield stress is determined by the 0.2% offset method. In this method, a line with a slope equal to the elastic modulus and a strain-intercept of 0.002 is plotted. The yield stress, σ_y , is the point where this line intersects the stress-strain curve. The UTS is simply the curve's maximum stress value. Note that this can occur at any point along the curve, not necessarily at failure. Finally, the ultimate strain, ϵ_u , is the material's strain at failure.

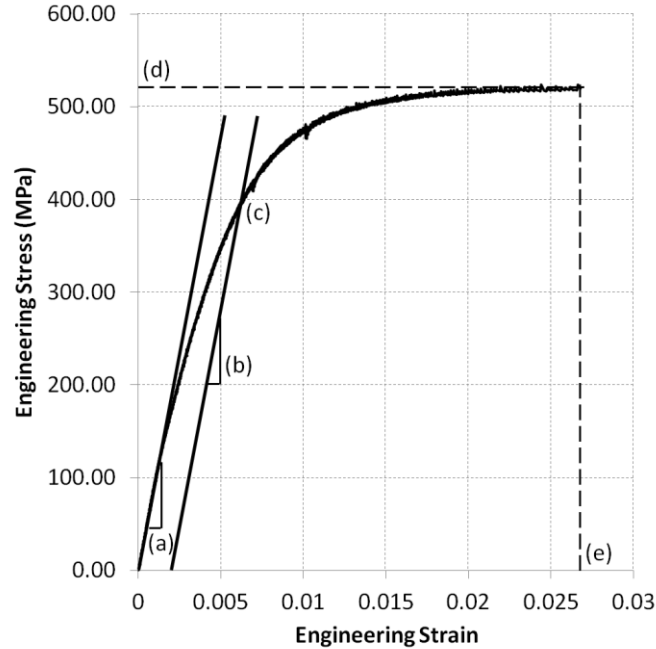


Figure 6. (a) Elastic modulus, (b) 0.2% offset line, (c) yield stress, (d) UTS, (e) ultimate strain. Curve is from a 30% CG ratio, longitudinal, 1 mm thick specimen tested at 293 K and 10^{-5} s^{-1} .

To provide insight into the variables that influence the mechanical behavior of the material while reducing the necessary number of experiments, an analysis of variance (ANOVA) procedure was used to examine the statistical significance of the effects. ANOVA attributes variance in a particular value to different sources. Thus, it helps to determine whether the mean values of two or more groups are statistically equal. The results of the analysis are the F-test statistic F which compares the amount explained variance to the amount of unexplained variance. This is then used to calculate a probability, p , that the means are equal, or equivalently, that the null hypothesis is true (i.e., the factor in question has no effect). A lower p -value indicates a stronger correlation, or a smaller chance that there is no effect [47]. The ANOVA results for the main effects examined later in this chapter are presented in Table 4.

Table 4
ANOVA Results for Main Effects

	<i>E</i>		σ_y		<i>UTS</i>		ϵ_u	
	<i>F</i>	<i>p</i>	<i>F</i>	<i>p</i>	<i>F</i>	<i>p</i>	<i>F</i>	<i>p</i>
CG Ratio	5.50	0.005	2.82	0.063	1.10	0.336	4.31	0.015
Temperature	42.71	0.000	267.10	0.000	438.19	0.000	293.43	0.000
Direction	5.11	0.025	33.99	0.000	41.19	0.000	153.80	0.000
Thickness	27.84	0.000	0.66	0.416	1.93	0.166	2.66	0.105
Strain Rate	0.56	0.455	4.57	0.034	7.61	0.007	8.31	0.005

In order to preserve the clarity of the discussion, the results presented below are for room temperature tests unless otherwise noted. Section 4.5 deals with the direct effects of temperature as well as the interactions between temperature and the other effects.

4.1 CG Ratio Effects

Figures 7 and 8 show the effect of CG ratio on the material's yield strength, UTS, and ductility. The material's increase in ductility with increasing CG ratio was expected; this is the very reason for the presence of the CGs to begin with. Likewise, the small decrease in strength was expected from the literature. The interesting feature of these figures is that, over the range tested, the effect of CG ratio appears to become saturated. This is illustrated most vividly in the graph for ultimate strain, which increases drastically between 10% and 20% but shows no significant change between 20% and 30%. The increase in yield strength and decrease in ultimate strain at 30% shown in the figure is not significant ($p \gg 0.05$) and within the scatter of the data.

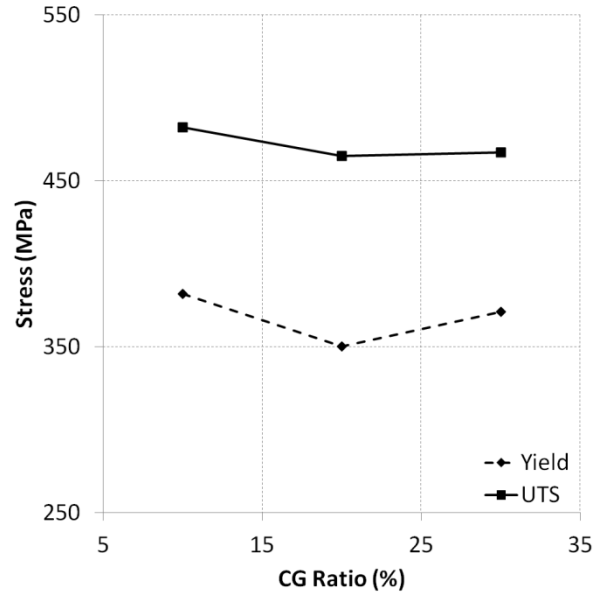


Figure 7. Effect of CG ratio on strength in the longitudinal direction.

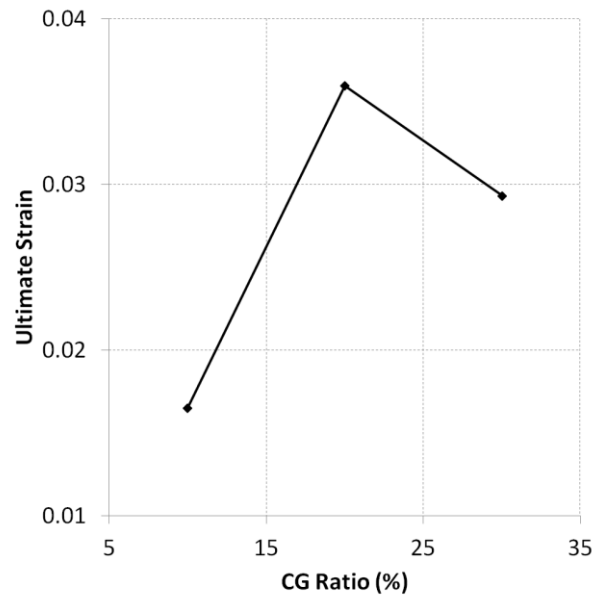


Figure 8. Effect of CG ratio on ductility in the longitudinal direction.

The coarse grains serve to increase ductility by retarding crack propagation in the UFG matrix where they initiate either by blunting the cracks or by delamination of the interface between the CG and UFG region [13]. A CG region embedded in the UFG matrix is shown in Figure 9. Some delamination is apparent, as well as a large amount of necking. As the CG ratio increases, the coarse grained regions cease to be discrete and begin to commingle. Thus, the

ability of the CGs to arrest cracks becomes “saturated” as the CG ratio increases. A finite element analysis (FEA) study of crack propagation in this material (Figure 10) has shown that the crack nucleates at a CG/UFG interface and tends to spread through the CG region first and move into the matrix only after the CG region has failed. When the CG ratio increases, the distances between the CG regions decreases and it becomes easier for the crack to propagate [48].

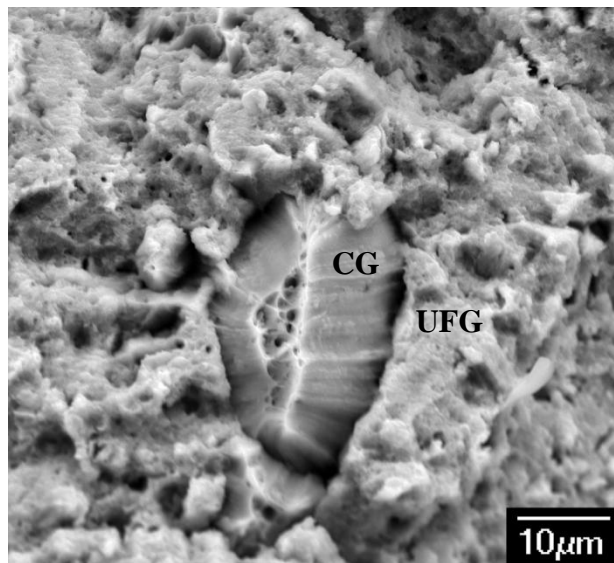


Figure 9. CG region in the UFG matrix on the fracture surface of a 10% CG material.

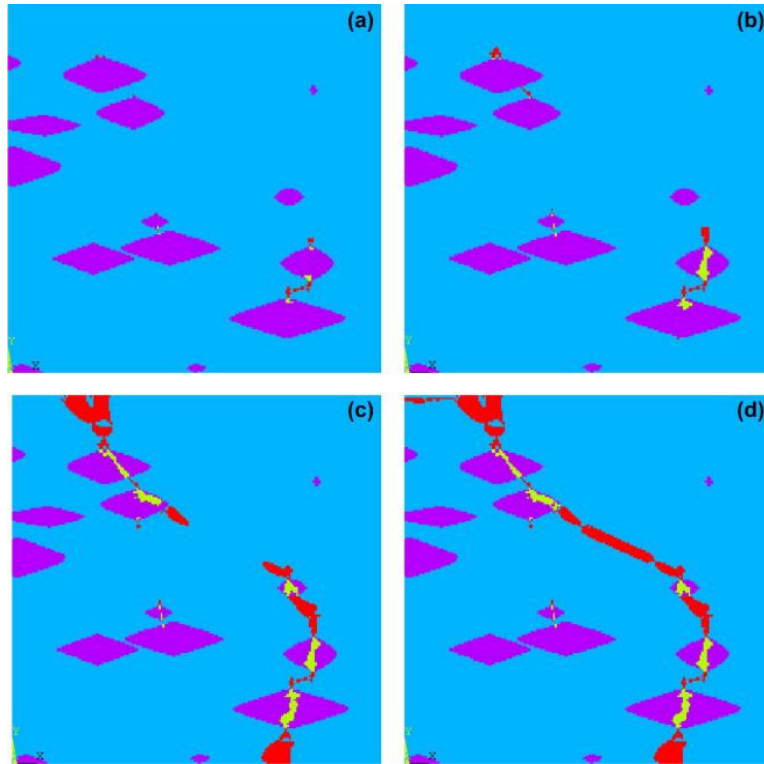


Figure 10. (a-d) FEA simulation of crack propagation. Purple areas are CGs, blue areas are UFGs. Red/green elements have failed. [48]

4.2 Anisotropy Effects

Anisotropy is a common result of the extrusion process, with the material typically showing reduced strength and ductility in the transverse direction [30]. These effects are attributed to mechanical fibering, elongation of a material's microstructure in the direction of extrusion. Mechanical fibering has been found to reduce the strength and ductility of extruded materials tested in the transverse direction [31,49].

This material conforms to this generalization, with the test results show that transverse specimens are weaker and less ductile than specimens cut in the longitudinal direction, shown in Figures 11 and 12. Unlike in the longitudinal direction, increasing CG ratio in the transverse direction actually serves to strengthen the material. However, the saturation of the CG ratio's effect above 20% that was noted in the longitudinal direction is still present. While increasing

CG ratio served to increase the ductility of the transverse specimens, their ultimate strain is still substantially lower than that of the longitudinal specimens. The stress-strain curves of the transverse tests showed little to no plastic deformation, shown in Figure 13.

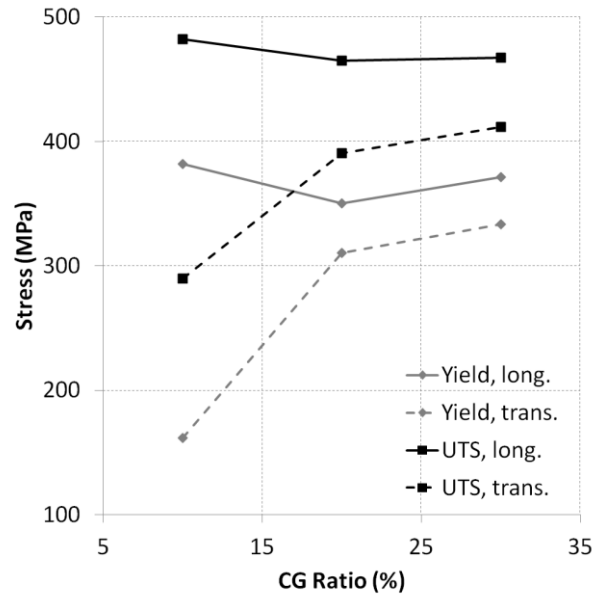


Figure 11. Effect of anisotropy and CG ratio on strength.

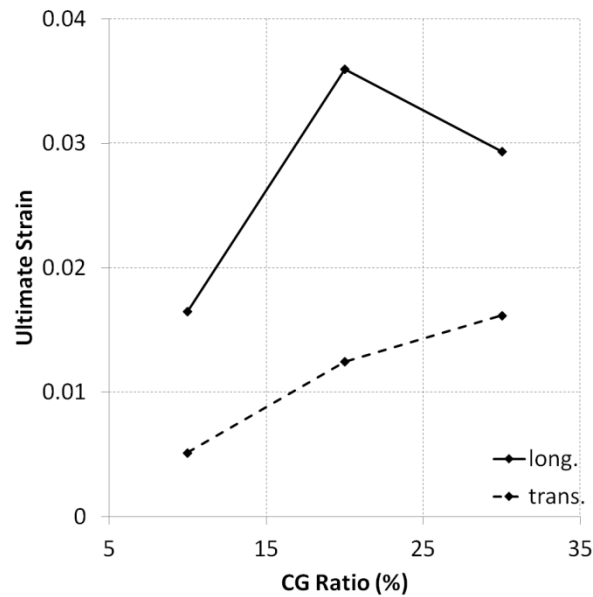


Figure 12. Effect of anisotropy and CG ratio on ductility.

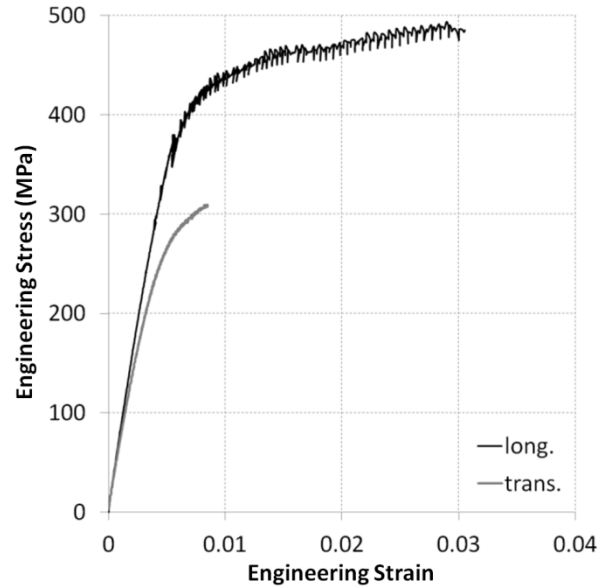


Figure 13. Tests at 20% CG ratio showing reduction in plasticity.

The increased strength with increasing CG ratio could be due to the limited amounts of plasticity that the material experienced when tested in the transverse direction. That is, in the transverse direction the material's failure was controlled by its ductility rather than its strength. Therefore, as the CG ratio was increased the material became more ductile allowing it to reach a higher stress before failing.

The transverse specimens' abrupt failure with little plasticity is suggestive of brittle-like failure. Observation of the failure profile with an optical microscope (Figure 14) supports this observation. Transverse specimens showed a smooth fracture surface perpendicular to the direction of the applied force that was unlike the jagged fracture surface found in the longitudinal specimens. SEM analysis of the failure surfaces (Figure 15) showed the characteristic "dimpled" morphology of ductile fractures in the longitudinal direction, while the transverse samples showed a grooved and intergranular fracture texture oriented in the direction of the extrusion [50]. Study of this fracture surface suggests that the transverse material failed at a variety of length scales. At larger scales it appears to have failed along PPBs left over from CIP and not

disrupted during the extrusion process. The finer features of the fracture surface are assumed to be due to the material failing along grain boundaries or groups of grain boundaries.

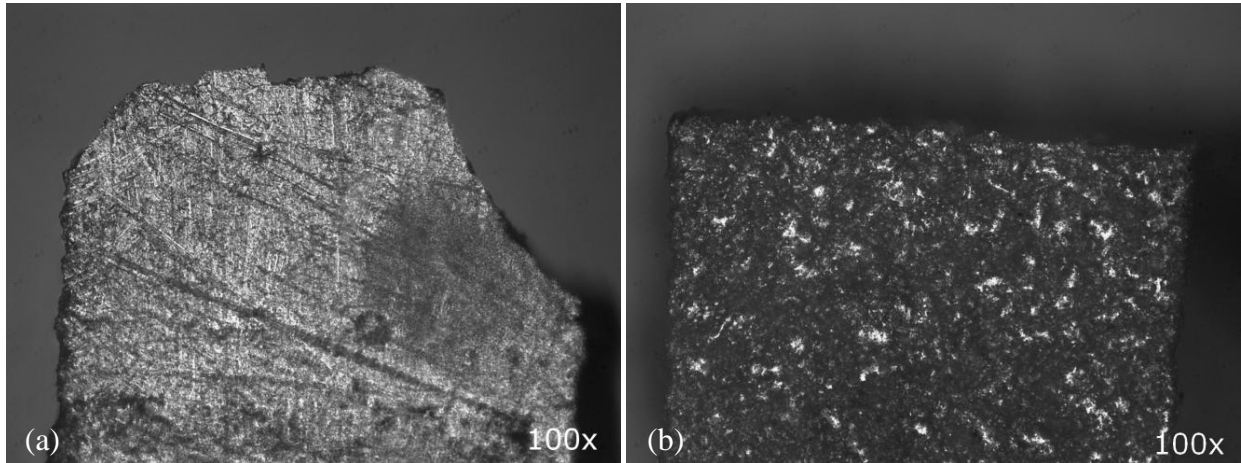


Figure 14. Optical micrographs of failure surfaces in profile of (a) longitudinal and (b) transverse specimens. The side of the longitudinal specimen shown here has been prepared for strain gauge application, while the transverse specimen shows the original EDM surface texture.

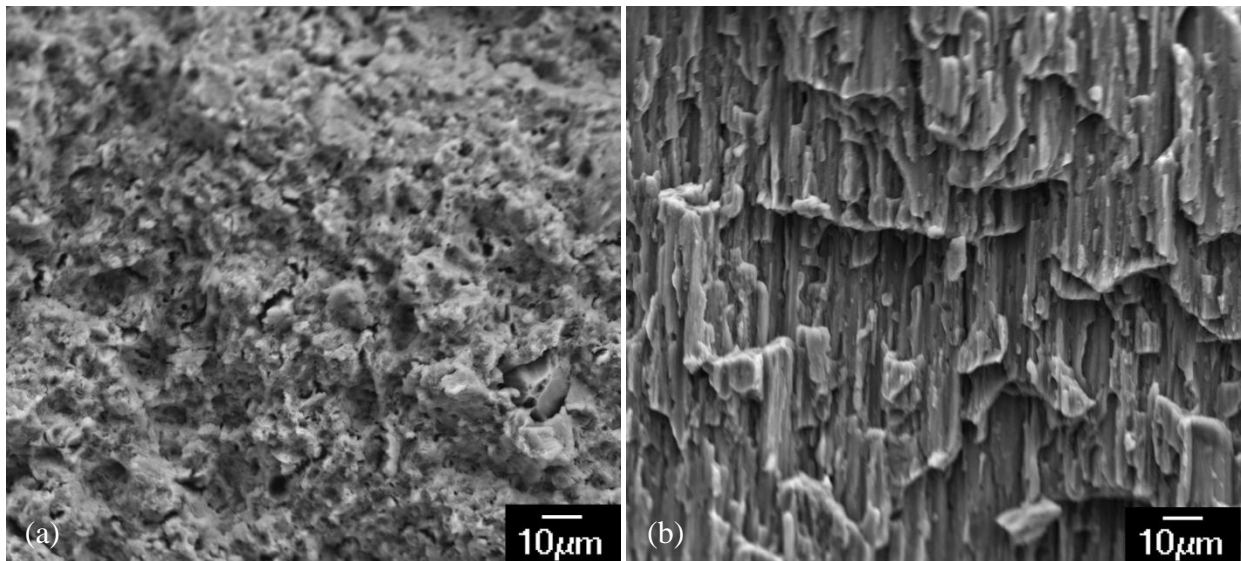


Figure 15. Scanning electron micrographs of fracture surfaces in (a) longitudinal and (b) transverse directions.

4.3 Strain Rate Effects

Compression tests of bimodal Al alloys have shown negative strain rate sensitivity [10,29]. That is, as strain rate increases, the strength of the material decreases. Likewise, the experimental results presented in Figures 16 and 17 also show a reduction in strength at higher strain rate. Typically this increase in strength at lower strain rates is accompanied by a loss of ductility. However, in this case ductility was observed to increase at the lower strain rate.

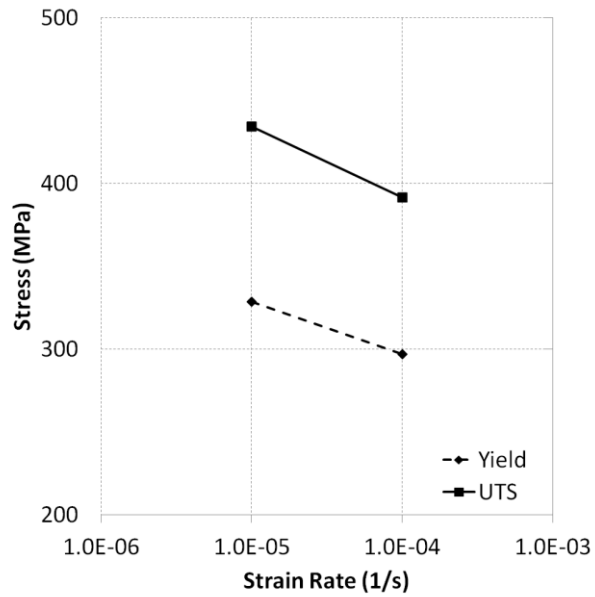


Figure 16. Effect of strain rate on strength.

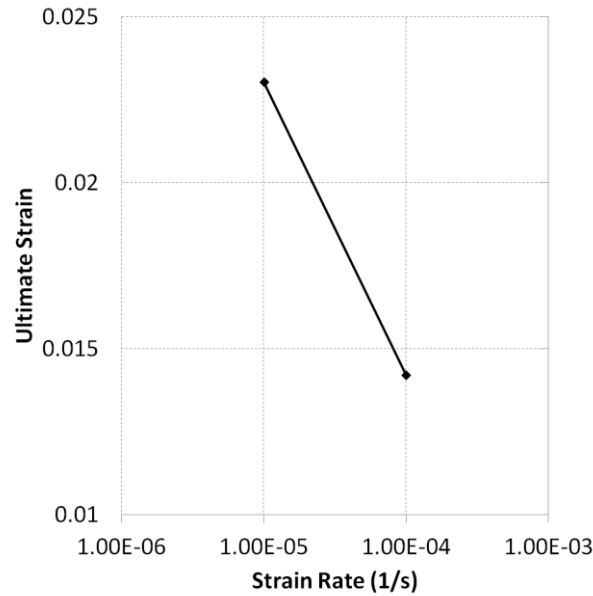


Figure 17: Effect of strain rate on ductility.

The effect of strain rate on strength is likely due to a phenomenon known as dynamic strain aging (DSA). DSA occurs when dislocations are temporarily blocked by obstacles in the material, such as solute atoms. This impediment to dislocation motion causes the material to become harder. The dislocations are more easily arrested at low strain rates, thus producing the observed negative strain rate sensitivity [51]. The stop and start nature of DSA gives rise to the Portevin-Le Chatelier effect, serrations in the stress-strain curve. Serrated stress-strain curves have been observed in other tests of bimodal Al as well as the tests presented here (Figure 18) [27,32].

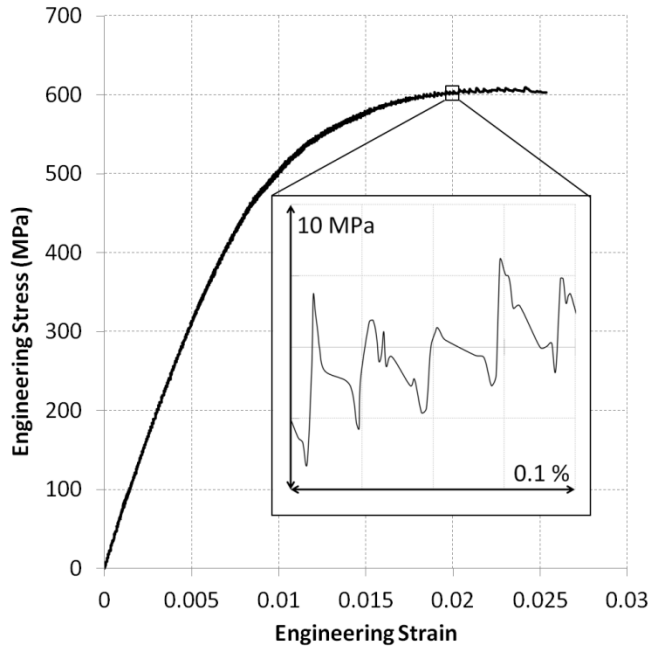


Figure 18. Enlarged section of a stress-strain curve from a test on a 0.5 mm longitudinal specimen at $1\text{E-}5 \text{ s}^{-1}$ showing serrations.

These results support the previously observed increased strength at slower strain rates. However, it is interesting to note that the ductility increased at lower strain rates, contrary to the findings of some of the aforementioned compression studies on bimodal Al [27,29]. As in this study, Han et al., found an increase in ductility at lower strain rates when conducting tensile tests on nanocrystalline Al-5083 [33]. As noted previously, most of the other strain rate tests conducted on this material have been compressive so this contradiction may be an effect of the test direction. In any event, this increased ductility is attributed to a “diffusion mediated stress relaxation mechanism” [33]. Lower strain rates allow more time for solute atoms to diffuse to local stress concentration sites where cracks would form and relax the stress in these areas. It should be noted that this is different from DSA in that the diffusing solute atoms interact with different features (dislocations vs. stress concentrations).

4.4 Thickness Effects

The specimen's thickness did not affect its strength or ductility. Surprisingly, the 1 mm thick specimens were found to have a significantly ($p < 0.01$) higher elastic modulus, shown in Figure 19. This effect was not expected and not easily explainable from a microstructural standpoint so further investigation was required.

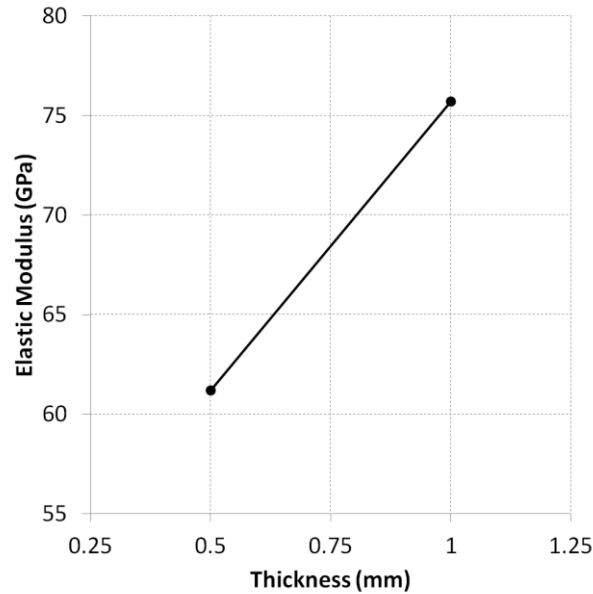


Figure 19. Effect of specimen thickness on elastic modulus.

To rule out the possibility of this effect being an inherent microstructural difference between specimens of different thicknesses, nanoindentation tests were performed on samples of the material at the two thicknesses. Nanoindentation is used to characterize the mechanical properties of small volumes of a material and can easily determine a material's elastic modulus. During a nanoindentation test, the load on the indenter and its displacement are recorded. This data is often represented as a load-depth curve, similar to the ones shown in Figure 20. Various aspects of these curves can be analyzed in order to extract the elastic and plastic behavior of the material. In this case, the initial slope of the unloading portion of the curve (the unloading stiffness, S) was studied as it can be related to the material's elastic modulus using the equation

$$E_r = \frac{\sqrt{\pi}}{2} \frac{S}{\sqrt{A_c}} \quad (\text{Eq. 2})$$

where E_r is the reduced elastic modulus, and A_c is the projected contact area [52]. The reduced elastic modulus is a value that combines the elastic modulus of the indenter and the specimen.

The material's elastic modulus can be extracted using the equation

$$\frac{1}{E_r} = \frac{(1-\nu^2)}{E} + \frac{(1-\nu_i^2)}{E_i} \quad (\text{Eq. 3})$$

where ν and E are the elastic modulus and Poisson's ratio of the material and ν_i and E_i are the elastic modulus and Poisson's ratio of the indenter [53].

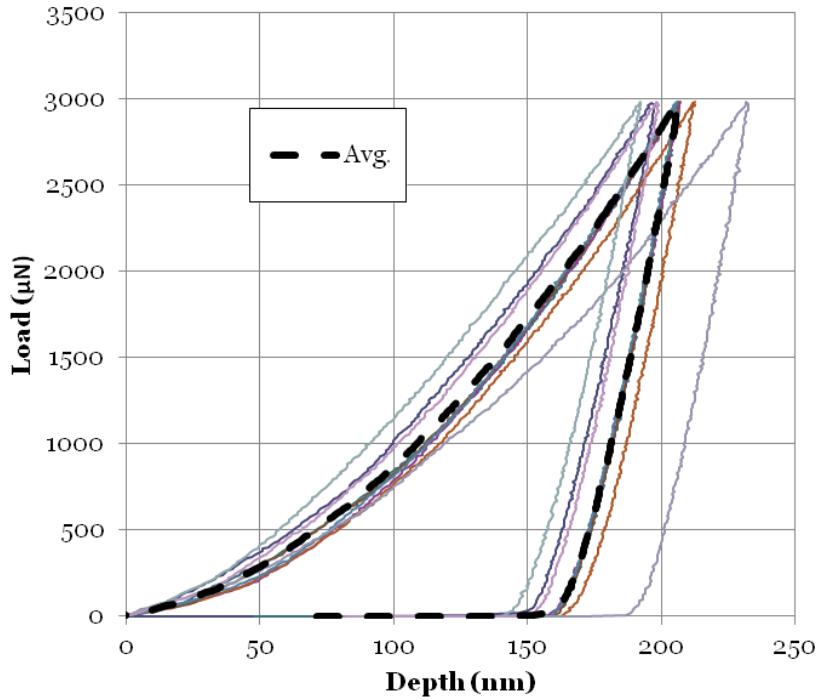


Figure 20. Load-depth curves from nanoindentation tests conducted on this material in [52].

The tests were carried out on a Hysitron TriboIndenter with a Berkovich indenter tip, which produces an indent like the one shown in Figure 21. On each sample, the elastic modulus was measured in four locations and averaged. These tests failed to find a difference in elastic modulus between the two samples ($p = 0.42$), so other causes were considered.

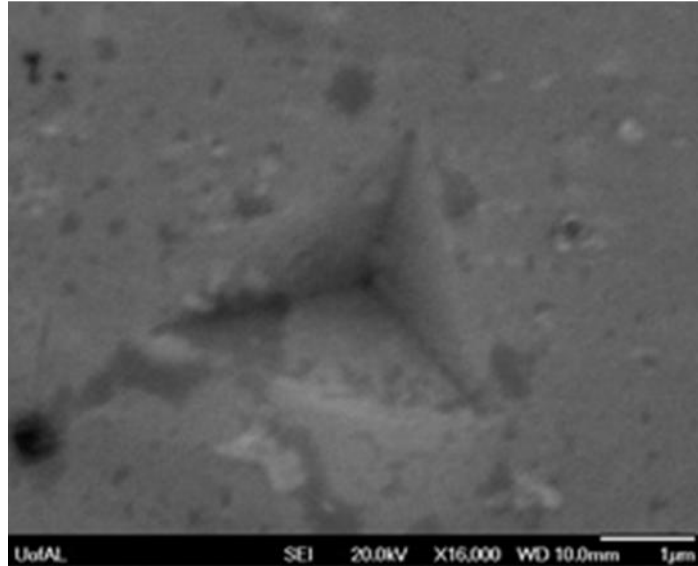


Figure 21. SEM image of an indent in this material presented in [52].

Another possible cause of this difference is the presence of a HAZ resulting from the EDM cutting procedure. EDM is known to produce a HAZ with properties different from the parent material. On large-scale parts, the HAZ is usually insignificant compared to the bulk material. As the size of the part is reduced, the volume of heat affected material makes up a larger portion of the part's total volume. Thus, it is conceivable that this may be responsible for the observed difference in elastic modulus.

The size and properties of the HAZ are known to vary based on a variety of factors and the properties of the HAZ may even vary based on depth [39,41,54-55]. This makes it difficult to predict its net effect on the material. Further study of the HAZ in this material would be necessary to determine its expected effects. However, if the HAZ was significant in these tests, it would intuitively be expected that other properties of the material would be affected [54]. Another possible cause for the elastic modulus discrepancy is a product of structural-mechanical effects due to either the specimen design or the tensile test set up or procedure. This is supported

by the observation that the material's other properties were not affected by the specimen's thickness.

Regardless of the ultimate cause, the conclusion that the specimen thickness does have some effect is supported not only by the ANOVA results, but also by observation of the fracture surface. SEM images of the fracture surfaces showed marked differences between 0.5 mm and 1 mm specimens, as shown in Figure 22. The 1 mm specimens showed a central region with a dimpled texture and a smoother "shear lip" region near the material edges. The thin specimens did not show the rough central region; the texture across the whole sample was like the edge texture of the thick specimens.

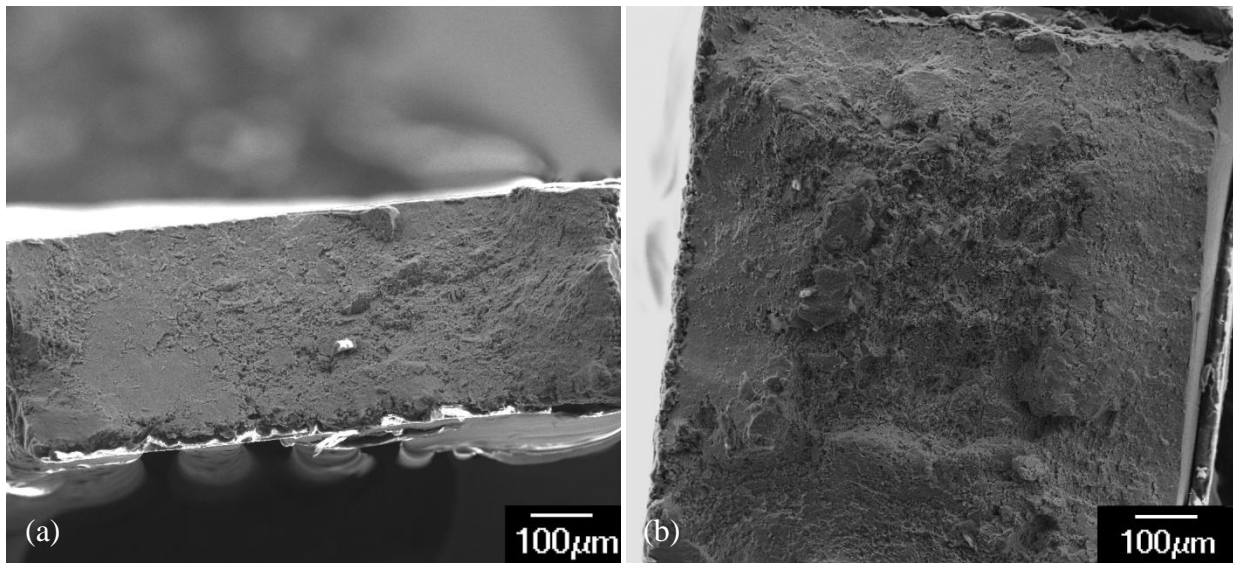


Figure 22. SEM images of fracture surfaces of (a) 0.5 mm and (b) 1 mm specimens in the longitudinal direction.

The differences in the failure surfaces are readily explained by the nature of ductile failure. When the specimen begins to neck, a hydrostatic stress field is created that causes voids to nucleate and grow in the middle of the material. These voids then coalesce to form a cavity in the center of the specimen, the result of which is the dimpled central region. When the crack approaches the edges of the material, it fails suddenly and creates the shear lip [56]. Thus, the

thicker specimens have more room for the central region to form before the crack approaches the specimen surface and fails.

4.5 Temperature Effects

As discussed in Appendix B, the range of the strain gauge recorder was extended in order to capture a larger portion of the plastic region. This was sufficient to record the entirety of the tests at room temperature. However, the increases in ductility at higher temperatures regularly went beyond even the extended range of the recorder, about 9% strain. Therefore, the observations of the effects of temperature on ductility presented here are qualitative and gathered from fractographic clues and observation of the tests.

EBSD images were taken of the material's microstructure of specimens tested at 293 and 473 K (Figure 23). The images were taken far from the gauge length to avoid any microstructural changes resulting from the material's deformation and not from the elevated temperature. Figure 24 shows the grain size distribution of the UFG region in both images. It can be seen here that there was no appreciable grain growth due to the test temperature.

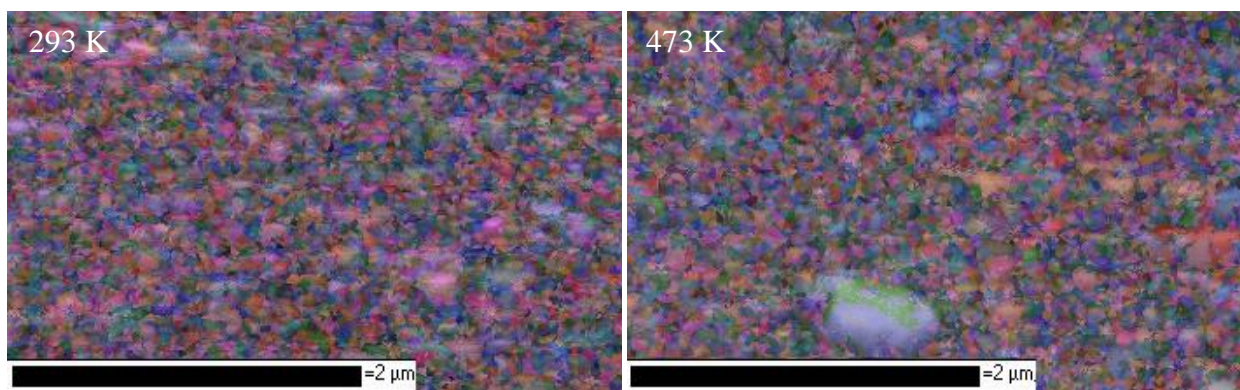


Figure 23. EBSD images of the microstructure in the transverse direction of specimens tested at 293 and 473 K.

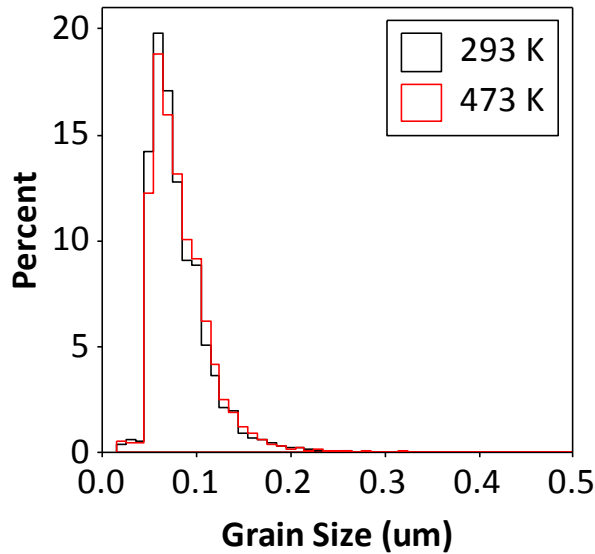


Figure 24. Histogram of grain size.

Figure 25 shows representative tests at the three test temperatures to compare the effect of temperature on the material's behavior. At higher temperatures, the material exhibited increased ductility, greater than 9%. Qualitative observation of the test results and failed specimens showed that ductility continued to increase between 383 and 473 K, though the exact magnitude of this effect could not be reliably determined.

The room temperature tests showed limited plastic deformation and high strength. As the material was heated it became much softer and more ductile as temperature increased, showing a perfectly plastic region after some work hardening at 383 K. At higher temperature, the stress peaked shortly after yielding then began to slowly decrease as strain increased, indicating dynamic recovery. As would be expected, the effect of dynamic recovery is more pronounced at higher temperature. As seen in Figure 26, the rate of recovery also appears to be affected by the CG ratio. The materials with lower CG ratio show greater recovery over the range studied.

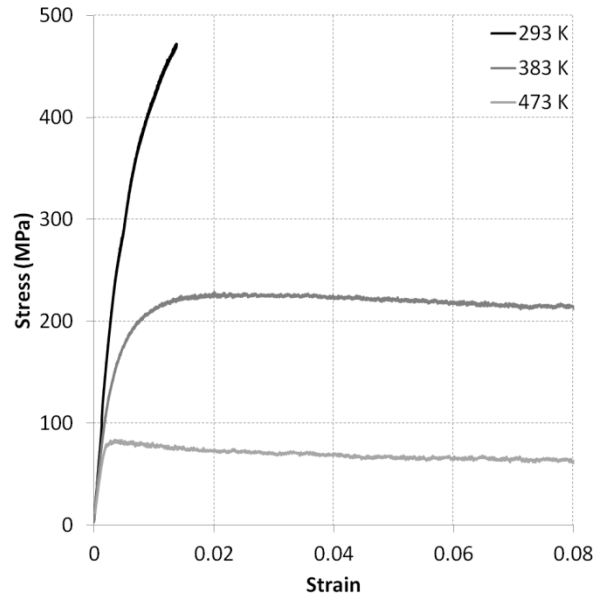


Figure 25. Effect of temperature on 10% CG material tested in the longitudinal direction at 10^{-5} s^{-1} .

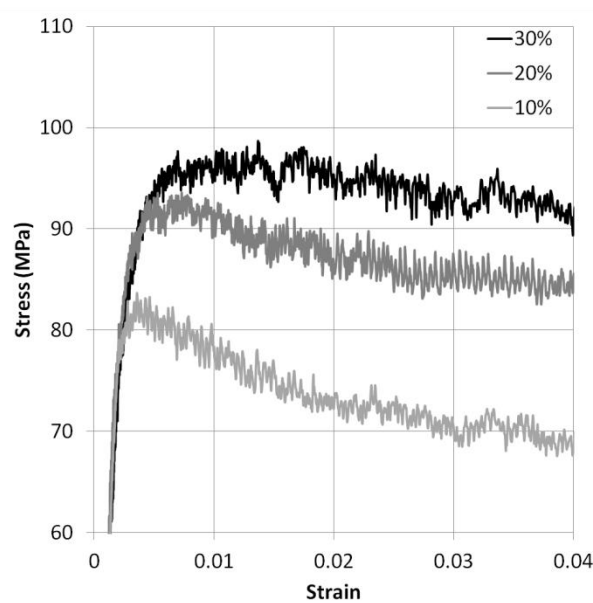


Figure 26. Enlarged view of the yield region of representative tests at 10^{-5} s^{-1} at 473 K at various CG ratios.

Recovery is driven by dislocations in thermodynamically unstable structures generated during deformation [57]. Thus, a material with a greater dislocation density has more thermodynamic “motivation” to recover. A TEM study conducted by the University of

California, Davis, on a sample of the 10% CG material tested at room temperature showed that the dislocation density was greater in the UFG regions [58]. Since the UFG volume decreases as CG volume increases, it is believed that the driving force was reduced at higher CG ratios, resulting in diminished recovery. Additionally, as CG ratio decreases, the UFG regions become more continuous, allowing the dislocations easier movement and promoting recovery.

Figures 27 and 28 show the effect of temperature on the 0.2% yield stress and ultimate stress of the material, compared among the different CG ratios and to the material's parent alloy, Al 5083. The effect of temperature appears to be uniform for all CG ratios tested. However, the bimodal material exhibits a drastically different response to increased temperature than the conventional alloy. The bimodal material also exhibits a more linear response to temperature, described by the equations

$$\sigma_y = 800 - 1.51T \quad (\text{Eq. 4})$$

$$UTS = 1090 - 2.09T \quad (\text{Eq. 5})$$

where T is temperature in K, σ_y is yield stress, and UTS is the ultimate tensile stress, both in MPa.

While the conventional material is much weaker at room temperature, it maintains its strength better at higher temperatures so that it is stronger than the bimodal alloy at 473 K. Higher temperature tests of 0% CG material have shown a similar trend when compared to a conventional alloy [45]. In these tests, the material's losses in strength begin to level out soon after about 473 K, though it remains weaker than the conventional material at the same temperature. The same pattern of greatly increased strength at room temperature coupled with no improvement compared to the conventional material at increased temperatures was also observed in a cryomilled Al-Mg-Sc alloy and a nanostructured Al 5083-Al₈₅Ni₁₀La₅ composite [59-60]. It

appears that the strengthening effect of grain size plays a diminishing role as temperature increases.

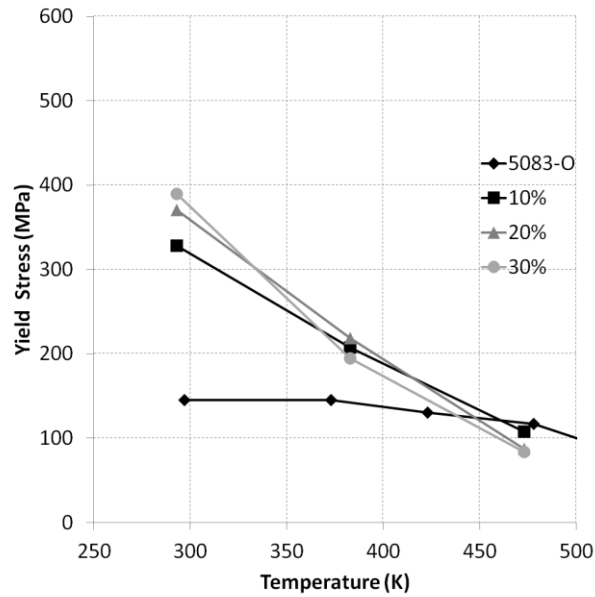


Figure 27. Effect of temperature on yield stress in the longitudinal direction. 5083-O data from [30].

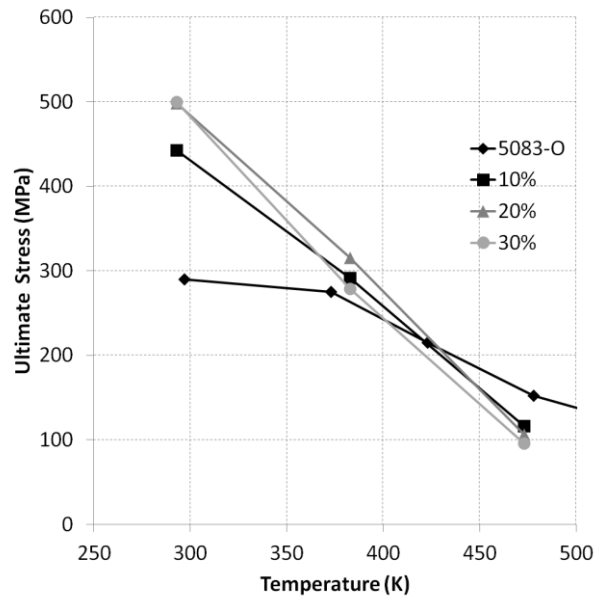


Figure 28. Effect of temperature on ultimate stress in the longitudinal direction. 5083-O data from [30].

Observation of the fracture surfaces under SEM (Figure 29) showed the effects of increased ductility at higher temperatures. As discussed in Section 4.4, the room temperature sample shows a clearly defined dimpled central region where voids nucleated and grew during plastic deformation surrounded by a shear lip region. When tested at higher temperature, the area of the central region grew and the shear lip region became less well-defined, until it disappeared altogether at the highest temperature. Also note how the dimples become larger as temperature increases. Evidence of increased plastic deformation at higher temperatures can also be seen in the bowing inward of the specimen's cross section in the 473 K image.

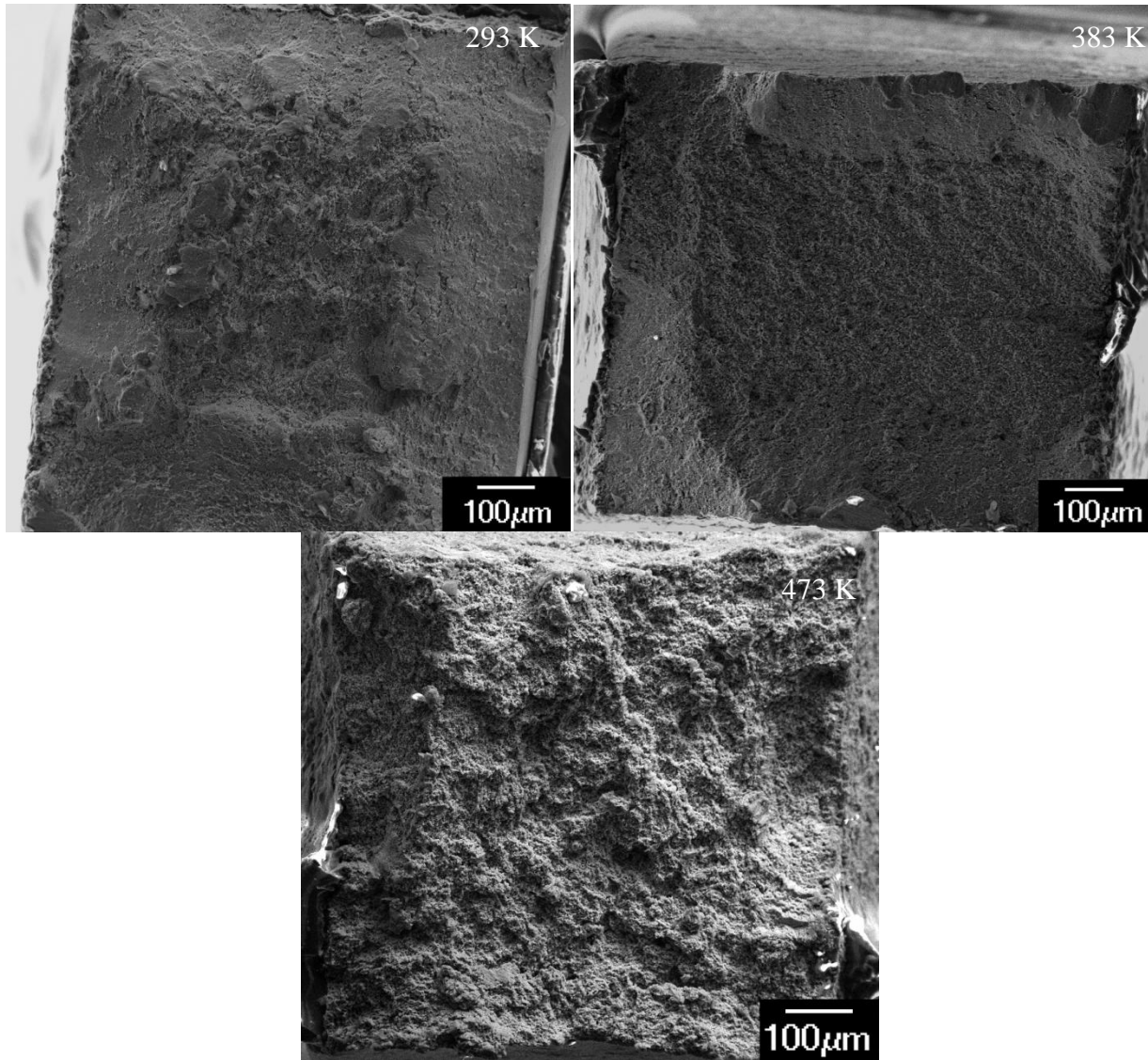


Figure 29. Longitudinal fracture surfaces from tests at different temperatures.

Figures 30 and 31 show how the strain rate effect changes with temperature. The negative strain rate sensitivity noted in Section 4.3 at room temperature can be seen in the slight increase in strength at the lower strain rate. As temperature increases to 383 K, the strain rate effect becomes positive. Then at 473 K, the material appears to be insensitive to strain rate. ANOVA shows this interaction effect to be significant with p -values of 0.047 for the yield strength and 0.007 for the ultimate strength.

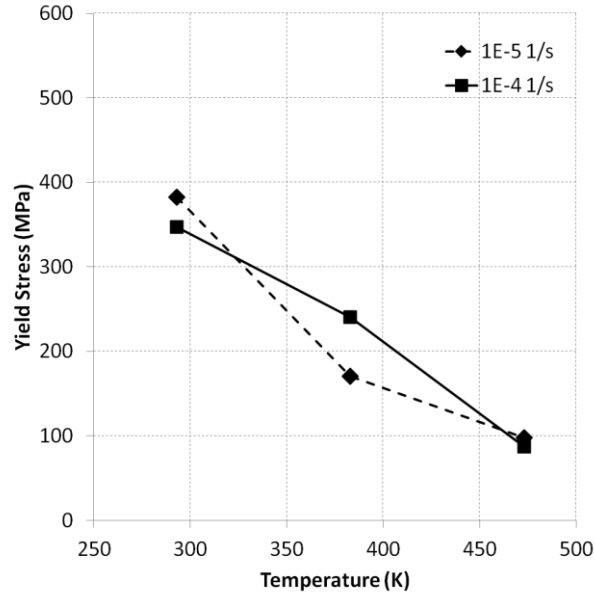


Figure 30. Interaction of strain rate and temperature effects on yield strength.

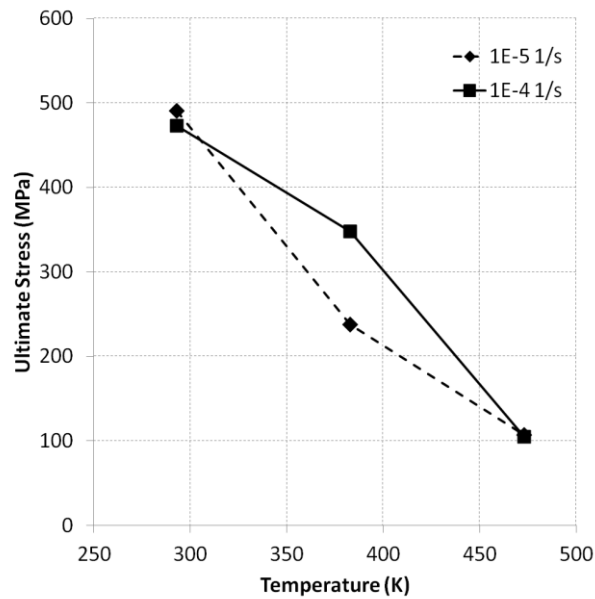


Figure 31. Interaction of strain rate and temperature effects on ultimate strength.

To quantify this observation, the strain rate sensitivity exponent was examined. The strain rate sensitivity exponent, m , is defined as

$$m = \left. \frac{d \ln(\sigma)}{d \ln(\dot{\epsilon})} \right|_{T, \epsilon}$$

where $\dot{\epsilon}$ is the strain rate and T is temperature. The strain hardening exponent was evaluated for the yield stress in the longitudinal direction at the three test temperatures and plotted in Figure 32.

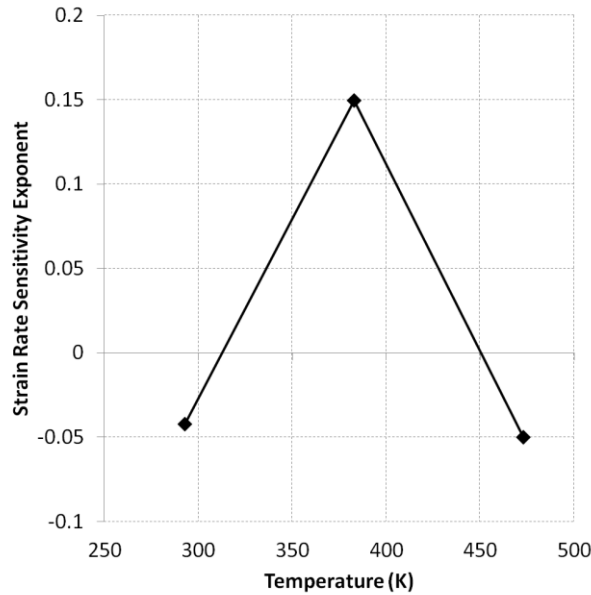


Figure 32. Strain rate sensitivity exponent as a function of temperature.

Initially, the strain rate sensitivity exponent behaved according to expectations. At room temperature, the exponent was slightly negative and it began to increase with temperature. However, as the temperature passed 383 K, the exponent decreased again to a slightly negative value instead of continuing to increase or at least remaining constant as has been previously observed in a similar compression test [43].

Further studies will have to be conducted to determine the nature of this effect. It is believed that the return of the strain rate sensitivity to a negative value at 473 K signifies the activation of new dislocation-blocking obstacles that were unable to diffuse effectively at room temperature. It would be expected that at higher temperatures, the strain rate sensitivity exponent would return to a positive value. Further investigation would be able to determine which obstacles to dislocation movement present in the material are active at a given temperature.

As illustrated in Figures 33 and 34, the anisotropic effects on strength that were observed in the room temperature tests became less significant as temperature increased. As described above, ultimate strains greater than 9% were not able to be recorded, so any temperature effects on the anisotropic ductility were difficult to quantify. However, the data presented in Table 5 suggest that the ductility of transverse specimens was still noticeably, though unquantifiably, lower than longitudinal ones. It is difficult to tell whether temperature is working to decrease or broaden the gap in ductility. What can be determined with certainty is that a difference in ductility exists and persists for all temperatures studied.

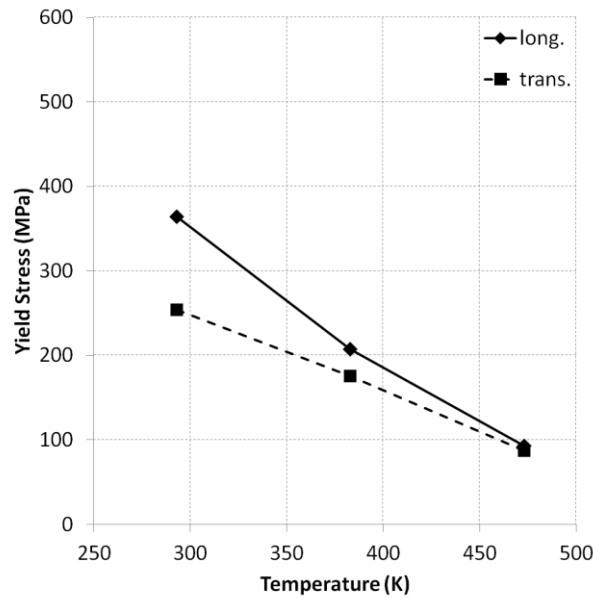


Figure 33. Effects of temperature and anisotropy on yield strength.

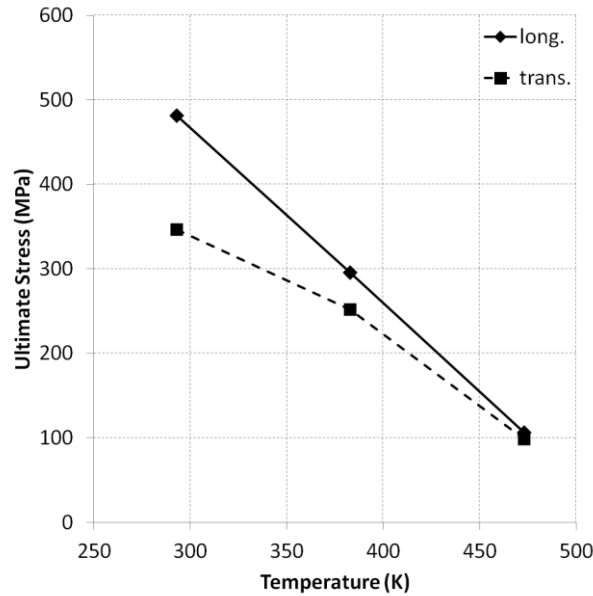


Figure 34. Effects of temperature and anisotropy on ultimate strength.

Table 5
Effect of Temperature on Ductility

Temperature [K]	Ultimate Strain [%]	
	Longitudinal	Transverse
293	2.8	1.0
383	>9.0	3.5
473	>9.0	>9.0

The differences in the fracture surfaces of the longitudinal and transverse specimens that were noted in Section 4.2 were also observed at higher temperatures (Figure 35). At higher temperature, the grooves of the transverse specimen's fracture surface became less well defined and started to show hints of dimpling. This is indicative of the extension of ductility and the plastic region observed in the transverse specimens as temperature increased. The continued differences in the fracture surfaces between the two directions support the idea that although the material starts to lose some anisotropy as temperature increases, at the temperatures examined in

this work, anisotropy continues to play a significant role in the determination of the material's properties.

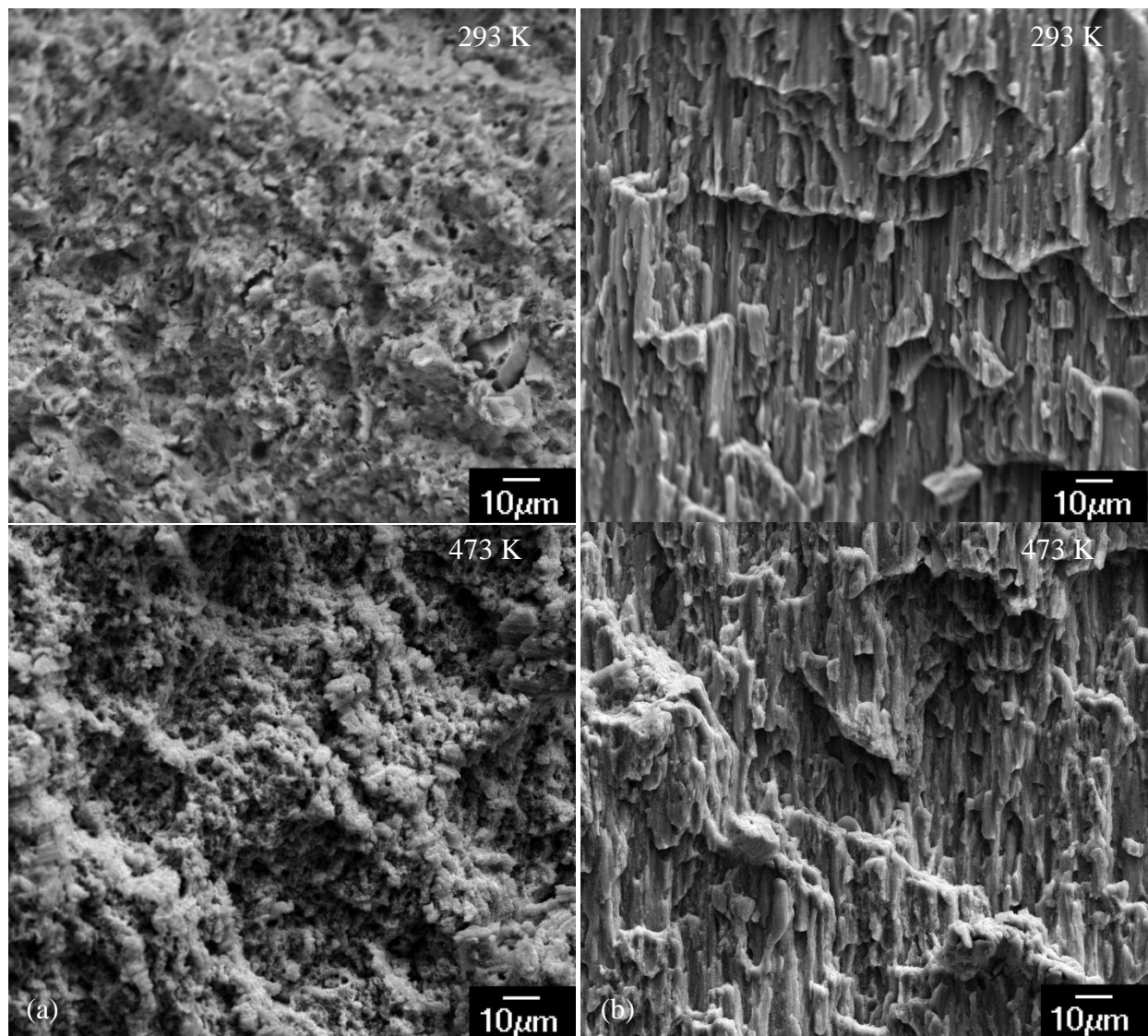


Figure 35. Fracture surfaces of (a) longitudinal and (b) transverse specimens.

CHAPTER 5

CONSTITUTIVE MODEL

At room temperature, the material's behavior was found to be described adequately by a combination of Hooke's law in the elastic region and Joshi's model for plasticity, shown in Equation 6 [61].

$$\sigma_f = \sigma_s - (\sigma_s - \sigma_j)e^{-\varepsilon_p/\varepsilon_c} \quad (\text{Eq. 6})$$

where σ_f is the flow stress, σ_s is the saturation stress, σ_j is the stress at the start of the plasticity model, ε_p is the plastic strain, and ε_c is the characteristic strain. The saturation stress and characteristic strain were determined for each set of data by performing a least-squares regression.

The start of the plasticity model, σ_j , can be thought of as a yield stress and is defined as the stress at which plastic deformation becomes appreciable [62]. Thus, σ_j was taken to be the point at which Hooke's law no longer adequately describes the stress-strain curve, that is, when the curve becomes nonlinear. This point was read from the experimentally determined stress-strain curve by fitting a line to the elastic region and then noting the point where the experimental curve began to deviate from the fit line. In this material at least, this stress is different enough from the 0.2% yield stress that is commonly reported that the two are not interchangeable. Both stresses are presented as they are useful in different ways but care is taken to distinguish the two.

The saturation stress is the final constant stress value that the model approaches as strain increases indefinitely [62]. While the saturation stress and UTS are similar, it should be kept in mind that they are not equivalent. The UTS is a physical property of the material, while the saturation stress is essentially just a number that helps to describe the behavior of the material. Thus, the two values in some cases may not show the same responses to an experimental factor. The characteristic strain is a proportionality constant that describes the shape of the plastic region. A smaller characteristic strain indicates that the model approaches the saturation stress more quickly.

Because Joshi's model only describes strain hardening, this model was found to be less useful at higher temperatures due to the presence of dynamic recovery effects (see Section 4.5). Thus, the constitutive model developed is only valid for the room temperature behavior of the material.

When combined with Hooke's law, the constitutive model for this material becomes

$$\begin{cases} \sigma = E\varepsilon & 0 < \varepsilon < \varepsilon_j \\ \sigma = \sigma_s - (\sigma_s - \sigma_j)e^{-\varepsilon_p/\varepsilon_c} & \varepsilon_j < \varepsilon < \varepsilon_u \end{cases} \quad (\text{Eq. 7})$$

where E is the elastic modulus, ε_j is the Joshi yield strain which can be found by calculating σ_j/E , and ε_u is the ultimate strain. As shown in Figure 36, this model was found to fit the experimental results well. The average model parameters for the conditions evaluated in this test are shown in Table 6.

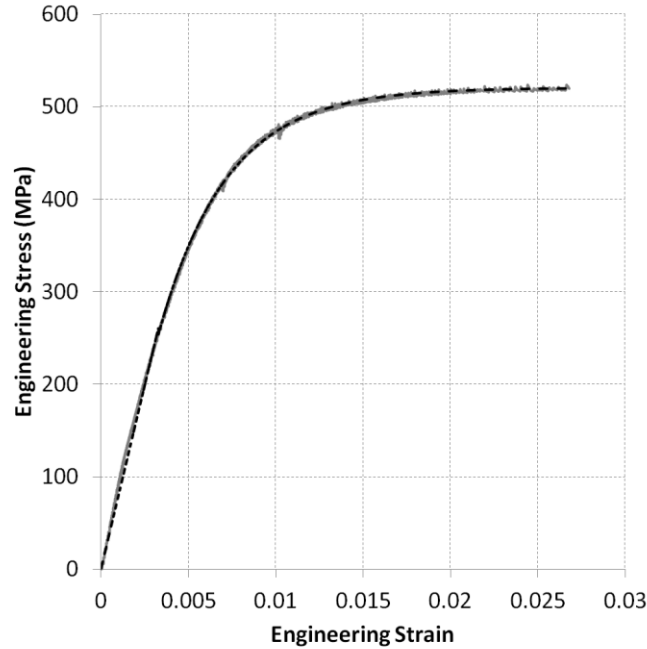


Figure 36. Model fit to the experimental data from a 30% longitudinal 1 mm specimen tested at 10^{-5} s^{-1} .

Table 6
Average Model Constants

	CG Ratio			Direction		Thickness [mm]		Strain Rate [s ⁻¹]	
	10%	20%	30%	Long.	Trans.	1	0.5	10 ⁻⁴	10 ⁻⁵
E [GPa]	66.8	71.8	68.0	69.7	68.0	75.9	61.9	69.0	68.7
σ_j [MPa]	221	117	167	183	120	163	153	161	155
σ_s [MPa]	526	444	448	478	438	457	467	449	475
ϵ_c	0.0054	0.0049	0.0043	0.0046	0.0050	0.0043	0.0052	0.0045	0.0050
ϵ_u	0.011	0.024	0.023	0.028	0.011	0.020	0.019	0.015	0.023

Many of the effects discussed in Chapter 4 can also be seen in the table, reflecting the accuracy of this model in depicting the material's behavior. It was found that for any given test at room temperature, the model fit the experimental data very well. Because of experimental scatter, however, when taken as a composite, the models are less of an accurate representation of

any single experimental curve. Rather, they depict the average behavior of the material for that set of conditions.

By taking into account data that was not affected by the changing conditions, Table 6 can be collapsed into a version that makes it easier to find the model parameters for a given set of conditions. The parameters that proved to be invariant with respect to the test conditions, namely elastic modulus and characteristic strain, are considered first. As discussed in Section 4.4 and shown in Table 6, the elastic modulus was found to vary with specimen thickness. However, it was determined that this was not an intrinsic property of the material but rather a side effect resulting from structural-mechanical effects of the testing procedure or specimen design. Thus, it is convenient to take the average elastic modulus of all tests, 69 GPa, as the value for all test conditions. The same logic can be applied to the characteristic strain to obtain a value of 0.005. The remaining data can now be presented in Table 7. Using this table in conjunction with the model presented in Equation 7, one can easily and accurately recreate the material's behavior for a given set of conditions.

Table 7
Reduced Table of Model Constants

	Longitudinal						Transverse					
	10^{-5} s^{-1}			10^{-4} s^{-1}			10^{-5} s^{-1}			10^{-4} s^{-1}		
	σ_j	σ_s	ϵ_u									
10%	243	558	1.9	199	493	1.4	168	569	0.6	235	433	0.4
20%	123	444	4.1	134	446	3.1	103	433	1.4	113	447	1.1
30%	182	466	4.0	219	466	2.1	128	467	1.9	144	397	1.9

σ_j, σ_s , in MPa; ϵ_u in %

CHAPTER 6

CONCLUSIONS

6.1 Effects of Test Parameters

A full-factorial experiment was designed and implemented to determine the effects of strain rate, specimen size, anisotropy, CG ratio, and temperature on a bimodal Al alloy in uniaxial tension. Through stress-strain data collected during the tests as well as post-test data gathered through fractography and microscopy, the following conclusions were drawn:

- Increasing the CG ratio of the material was found to increase its ductility and slightly lower its strength. The effect of adding CGs appears to become saturated at some point as there was little difference in the strength and ductility of the 20% and 30% CG materials.
- The material is anisotropic and exhibits drastically reduced strength and ductility when loaded in the transverse direction. The fracture surface between these two directions is also noticeably different.
- In the transverse direction, increasing CG ratio actually serves to increase the material's strength. This is believed to be due to the material's failure when loaded in the transverse direction being limited by ductility rather than strength.
- At room temperature, a small amount of negative strain rate sensitivity was observed. The stress-strain curve of the material was serrated, consistent with DSA effects. The ductility of the material was noted to increase at lower strain rates, attributable to a stress relaxation mechanism.

- There was no effect of specimen thickness on the strength or ductility of the material. However, a significant increase in elastic modulus was noted in the thicker specimens which was attributed to structural-mechanical effects inherent in the specimen design or testing apparatus. This highlights the necessity of care that should be taken when designing non-standard specimens.
- The material's strength decreased and ductility increased as temperature was increased from 293 to 473 K. At 473 K, the strength of this material is less than that of Al 5083 at the same temperature. Although ultimate strain often exceeded 9% and was thus not able to be measured, the observations of increased ductility are supported by fractographic evidence. The presence of dynamic recovery was noted, and the amount of recovery was observed to be dependent on CG ratio.
- The strain rate sensitivity of the material was found to depend non-monotonically on temperature. The strain rate sensitivity exponent was slightly negative at 293 and 473 K but solidly positive at 383 K.
- The anisotropic effects on the material's strength were observed to become less significant as temperature increased. However, the textural differences in the material's fracture surface were largely maintained, with some indications of increased ductility.
- EBSD analysis failed to find a significant amount of grain growth in tests conducted at high temperature compared to tests at room temperature.

At room temperature, the material's behavior was found to conform well to a combination of Hooke's law and Joshi's plasticity model. A constitutive model was developed to describe the effects of the test parameters on the material's properties. Because of dynamic recovery, this model was not as accurate at describing the material's high temperature behavior.

6.2 Contribution

This work has added to the understanding of how the mechanical properties of bimodal materials, this alloy in particular, respond to changes in their testing conditions. This knowledge can be extended to the use of these materials in design applications. The material presented here also broadens the knowledge of why these materials behave in the manner they do, allowing for them to be more intelligently engineered in the future. The constitutive model developed provides a starting point for the development of finite element simulations incorporating this material. Finally, this work serves to demonstrate a method of performing tensile tests on miniature, non-standard specimens as well as highlighting some challenges that may arise from the use of such specimens.

6.3 Future Work

This study provided a basis for the exploration of the effects present in this material. Larger and different parameter ranges than those used in this work should be investigated in order to have a broader understanding of this material's behavior under all conditions. Other possible effects which were not considered here, such as creep, should be examined.

A major question raised by this work but ultimately left unanswered was that of the nature of the strain rate sensitivity's dependence on temperature. This effect does warrant further study and consideration in order to develop a more complete knowledge of this material. Likewise, experimental work should be carried out in order to examine the theories presented here to explain the effect of thickness on the measured elastic modulus. In this and other areas, this work has also highlighted the need for the development and implementation of standard specimen designs and testing procedures for very small specimens.

APPENDIX A

SPECIMEN AND TEST FIXTURE DESIGN

The test specimens used in this study had some unique requirements imposed upon them. They had to conform to the dimensions of the extruded rod, which was about 2 cm in diameter. Since it is desirable to use the same specimens in the longitudinal and transverse directions, the entire length of the specimen, including the grip area and gauge length, could not exceed 20 mm. This, and the fragility of such a small amount of material, precluded the use of many commercially available tensile test grips. Thus, compatible grips also had to be designed.

Early specimen designs were plagued with problems including slipping out of the test fixture when a load was applied and not breaking in the gauge length (Figure 37). To combat both of these problems, a new specimen was designed that maximized the grip area while minimizing the width of the gauge area. The cross section of the gauge area was made non-uniform in order to avoid the stress concentrations that had been causing the previous designs to break in unwanted ways.



Figure 37. (left, middle) Old specimen designs showing unwanted failure locations. (right) Final specimen design with an acceptable failure location.

To accommodate the specimen's small size, custom tensile grips were designed and produced. These grips, shown in Figure 38, were designed to allow the specimens to be easily fixed in spite of their small size, while still being able to impart a sufficient force upon them. This was accomplished by using bolts to clamp the specimen between the two halves of the grip. The inside surfaces of the halves were grooved to allow the grips to maintain their hold on the specimen and prevent slipping.



Figure 38. Tensile grips.

The specimen's unconventional design was found to perform as intended. The final design of the specimen was found to solve these problems and still produce reliable data, attested to by comparison of the data presented here with Table 2. However, as evidenced by the discrepancies in elastic modulus discussed in Section 4.4, using non-standard specimens carries an inherent risk and such specimens should be used carefully.

APPENDIX B

EXTENDING THE RANGE OF THE P3 STRAIN GAUGE RECORDER

From the factory, the Vishay P3 recorder has an upper limit of about 30,000 $\mu\epsilon$. The increases in ductility associated with the higher temperature tests was often enough to go beyond the instruments capabilities. The recording range of this instrument can be extended by adding attenuating resistors to the signal wires in series with the strain gauge (Figure 39), thereby “cutting” the signal and increasing range at the cost of resolution. The relationship between the size of the attenuating resistors and the increase in the instrument’s range is described by Equation 8.

$$r_{ext} = \frac{(R_{att} + R_G + R_L)}{R_G} \quad (\text{Eq. 8})$$

where r_{ext} is the factor that the range is extended by, R_{att} is the value of the attenuating resistors, R_G is the gauge resistance (120 Ω for the gauges used in these experiments), and R_L is the lead wire resistance (assumed to be negligible) [63].

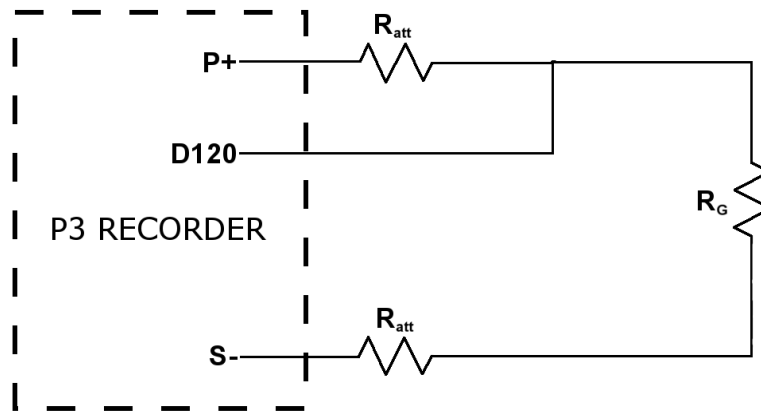


Figure 39. Placement of attenuating resistors in a quarter-bridge configuration.

The implementation of this procedure to increase the range has an unfortunate side effect of causing the recorder to no longer record “true” strain; that is, the strains shown on the instrument are reduced by the same factor that the range is increased by (a strain of 15,000 $\mu\epsilon$ is displayed as 5,000 $\mu\epsilon$ for a 3x range extension). However, this can easily be compensated for by reducing the gauge factor given to the P3 by the same factor that the range was increased. For example, if the range was extended by a factor 3 and the strain gauges used have a gauge factor of 2.15, the gauge factor input to the P3 should be $2.15/3 = 0.717$ [63].

In this study, 240 Ω precision resistors were added to extend the recorder’s range by a factor of 3, for a maximum strain of 90,000 $\mu\epsilon$ or 9%. This resistance value was chosen because it caused the instrument’s maximum to be near the strain gauge/adhesive installation’s maximum of about 10%.

REFERENCES

- [1] Petch, N.J. "The Cleavage Strength of Polycrystals" *J. Iron and Steel Inst.*, 25 (1953).
- [2] Carlton, C.E. and Ferreira, P.J. "What is behind the inverse Hall–Petch effect in nanocrystalline materials?" *Acta Materialia* 55 no. 11, 3749-3756 (2007).
- [3] Newbery, A.P., Ahn, B., Hayes, R.W., Pao, P.S., Nutt, S.R. and Lavernia, E.J. "Consolidation and Forging Methods for a Cryomilled Al Alloy" *Metallurgical and Materials Transactions A* 39 no. 9, 2193-2205 (2008).
- [4] Newbery, A.P., Ahn, B., Pao, P., Nutt, S.R., and Lavernia, E.J., "A Ductile UFG Al Alloy via Cryomilling and Quasi-Isostatic Forging," *Advanced Materials Research* 29-30, 21-29 (2007).
- [5] Newbery, A.P., Ahn, B., Topping, T.D., Pao, P.S., Nutt, S.R., and Lavernia, E.J. "Large UFG Al alloy plates from cryomilling," *Journal of Materials Processing Technology* 203, 37-45 (2008).
- [6] Tellkamp, V.L. and E.J. Lavernia "Processing and mechanical properties of nanocrystalline 5083 Al alloy." *Nanostructured Materials* 12, 249-252 (1999).
- [7] Topping, T., Ahn, B., Ying, L., Nutt, S.R. and Lavernia, E.J. "Influence of Process Parameters on the Mechanical Behavior of an Ultrafine-Grained Al Alloy," *Metallurgical and Materials Transactions A*, 1-15 (2011).
- [8] Youssef, K.M., Scattergood, R.O., Murty, K.L. and Koch, C.C. "Nanocrystalline Al–Mg alloy with ultrahigh strength and good ductility" *Scr.Mater.* 54, no. 2, 251-256 (2006).
- [9] Han, B., Ye, J., Tang, F., Schoenung, J. and Lavernia, E. "Processing and behavior of nanostructured metallic alloys and composites by cryomilling" *J.Mater.Sci.* 42, no. 5, 1660-1672 (2007).
- [10] Witkin, D.B., and Lavernia, E.J., "Synthesis and mechanical behavior of nanostructured materials via cryomilling," *Progress in Materials Science* 51, 1-60 (2006).
- [11] Ahn, B.M., Lavernia E.J., and Nutt S.R., "Dynamic observations of deformation in an ultrafine-grained Al-Mg alloy with bimodal grain structure," *Journal of Materials Science* 43, 7403-7408 (2008).

- [12] Han, B.Q., Huang, Y.J., Zhu, Y.T., and Lavernia, E.J. "Strain rate dependence of properties of cryomilled bimodal 5083 Al alloys," *Acta Materialia* 54, no. 11, 3015-3024 (2006).
- [13] Han, B.Q., Lavernia, E.J., Lee, Z., Nutt, S., and Witkin, D. "Deformation behavior of bimodal nanostructured 5083 Al alloys" *Metallurgical and Materials Transactions A* 36A, no. 4, 957-965 (2005).
- [14] Lee, Z., Radmilovic, V., Ahn, B., Lavernia, E.J., and Nutt, S.R. "Tensile Deformation and Fracture Mechanism of Bulk Bimodal Ultrafine-Grained Al-Mg Alloy" *Metallurgical and Materials Transactions A* 41A, no. 4, 795-801 (2010).
- [15] Lee, Z., Witkin, D.B., Radmilovic, V., Lavernia, E.J., and Nutt, S.R. "Bimodal microstructure and deformation of cryomilled bulk nanocrystalline Al-7.5Mg alloy," *Materials Science and Engineering A* 410, 462-467 (2005).
- [16] Witkin, D., Lee, Z., Rodriguez, R., Nutt, S., and Lavernia, E. "Al-Mg alloy engineered with bimodal grain size for high strength and increased ductility," *Scripta Materialia* 49, no. 4, 297-302 (2003).
- [17] Li, Y., Zhao, Y.H., Ortalan, V., Liu, W., Zhang, Z.H., Vogt, R.G., Browning, N.D., Lavernia, E.J., and Schoenung, J.M. "Investigation of aluminum-based nanocomposites with ultra-high strength." *Materials Science and Engineering A* 527, 305-316 (2009).
- [18] Lucadamo, G., Yang, N.Y.C., San Marchi, C., and Lavernia, E.J., "Microstructure characterization in cryomilled Al 5083," *Materials Science and Engineering A* 430, no. 1-2, 230-241 (2006).
- [19] Li, Y., Liu, W., Ortalan, V., Li, W.F., Zhang, Z., Vogt, R., Browning, N.D., Lavernia, E.J., and Schoenung, J.M. "HRTEM and EELS study of aluminum nitride in nanostructured Al 5083/B4C processed via cryomilling" *Acta Materialia* 58, 1732-1740 (2010).
- [20] Ahn, B., Newbery, A.P., Lavernia, E.J., and Nutt, S.R., "Effect of degassing temperature on the microstructure of a nanocrystalline Al-Mg alloy," *Materials Science and Engineering A* 463, 61-66 (2007).
- [21] Newbery, A. P., Ahn, B., Topping, T. D., Pao, P. S., Nutt, S. R., and Lavernia, E. J., "Large UFG Al alloy plates from cryomilling," *Journal of Materials Processing Technology* 203, 37-45 (2008).
- [22] Walley, J. L., Lavernia, E. J., and Gibeling, J. C., "Low-Cycle Fatigue of Ultra-Fine-Grained Cryomilled 5083 Aluminum Alloy," *Metallurgical and Materials Transactions A* 40A, 2622-2630 (2009).
- [23] Tellkamp, V. L., Melmed, A., and Lavernia, E. J., "Mechanical Behavior and Microstructure of a Thermally Stable Bulk Nanostructured Al Alloy," *Metallurgical and Materials Transactions A* 32A, 2335-2343 (2001).

- [24] Lavernia, E.J., Han, B.Q., and Schoenung, J.M., "Cryomilled nanostructured materials: Processing and properties," *Materials Science and Engineering A* 493, 207-214 (2008).
- [25] Li, Y., Zhang, Z., Vogt, R., Schoenug, J.M., Lavernia, E.J. "Boundaries and interfaces in ultrafine grain composites." *Acta Materialia* 59, 7206-7218 (2011).
- [26] Liao, X.Z., Huang, J.Y., Zhu, Y. T., Zhou, F., Lavernia, E.J., "Nanostructures and deformation mechanisms in a cryogenically ball-milled Al-Mg alloy," *Philosophical Magazine* 83, no. 26, 3065 – 3075 (2003).
- [27] Fan, G.J., Wang, G.Y., Choo, H., Liaw, P.K., Park, Y.S., Han, B.Q. and Lavernia, E.J. "Deformation behavior of an ultrafine-grained Al–Mg alloy at different strain rates" *Scr.Mater.* 52, no. 9, 929-933 (2005).
- [28] Han, B.Q., Lee, Z., Nutt, S.R., Lavernia, E.J., and Mohamed, F.A., "Mechanical Properties of An Ultrafine-Grained Al-7.5 Pct Mg Alloy," *Metallurgical and Materials Transactions A* 34A, no. 3, 603-613 (2003).
- [29] Fan, G.J., Choo, H., Liaw, P.K. and Lavernia, E.J. "Plastic deformation and fracture of ultrafine-grained Al–Mg alloys with a bimodal grain size distribution" *Acta Materialia* 54, no. 7, 1759-1766 (2006).
- [30] *Metals Handbook: Desk Edition*, 2nd ed., American Society for Metals, Materials Park, OH (1998).
- [31] Han, B.Q., Lavernia, E.J. and Mohamed, F.A. "On the mechanical behavior of a cryomilled Al–Ti–Cu alloy" *Materials Science and Engineering A* 58, no. 1-2, 318-323 (2003).
- [32] Han, B., Mohamed, F., Lee, Z., Nutt, S. and Lavernia, E. "Mechanical properties of an ultrafine-grained Al-7.5 Pct Mg alloy" *Metallurgical and Materials Transactions A* 34, no. 3, 603-613 (2003).
- [33] Han, B.Q., Huang, J.Y., Zhu, Y.T. and Lavernia, E.J. "Effect of strain rate on the ductility of a nanostructured Al alloy" *Scr.Mater.* 54, no. 6, 1175-1180 (2006).
- [34] Hayes, R.W., Witkin, D., Zhou, F. and Lavernia, E.J. "Deformation and activation volumes of cryomilled ultrafine-grained Al" *Acta Materialia* 52, no. 14, 4259-4271 (2004).
- [35] Kim, G., Ni, J. and Koc, M. "Modeling of the Size Effects on the Behavior of Metals in Microscale Deformation Processes" *J.Manuf.Sci.Eng.* 129, no. 3, 470-476 (2007).
- [36] Miyazaki, S., Fujita, H. and Hiraoka, H. "Effect of specimen size on the flow stress of rod specimens of polycrystalline Cu-Al alloy" *Scripta Metallurgica* 13, no. 6, 447-449 (1979).
- [37] Miyazaki, S., Shibata, K. and Fujita, H. "Effect of specimen thickness on mechanical properties of polycrystalline aggregates with various grain sizes" *Acta Metallurgica* 27, no. 5, 855-862 (1979).

- [38] Janssen, P.J.M., Hoefnagels, J.P.M., de Keijser, T.H. and Geers, M.G.D. "Processing induced size effects in plastic yielding upon miniaturisation" *J.Mech.Phys.Solids* 56, no. 8, 2687-2706 (2008).
- [39] Lee, L.C., Lim, L.C., Narayanan, V. and Venkatesh, V.C. "Quantification of surface damage of tool steels after EDM" *Int.J.Mach.Tools Manuf.* 28, no. 4, 359-372 (1988).
- [40] Ramulu, M., Paul, G. and Patel, J. "EDM surface effects on the fatigue strength of a 15 vol% SiCp/Al metal matrix composite material," *Composite Structures* 54, no. 1, 79-86 (2001).
- [41] Guitrau, E.B., Recast Revisited, in EDM Today., Roger Kern: www.EDMtodayMagazine.com (2008).
- [42] Mallick, A., Vedantam, S., and Lu, L., "Grain size dependent tensile behavior of Mg-3%Al alloy at elevated temperatures," *Materials Science and Engineering A* 515, 14-18 (2009).
- [43] Witkin, D., Han, B.Q., and Lavernia, E.J., "Mechanical Behavior of Ultrafine-Grained Cryomilled Al 5083 at Elevated Temperature," *Journal of Materials Engineering and Performance* 14 no. 4, 519-527 (2005).
- [44] Huskins, E., Cao, B., Li, B., and Ramesh, K.T., "Temperature-Dependent Mechanical Response of an UFG Aluminum Alloy at High Rates," *Experimental Mechanics* 52, 185-194 (2012).
- [45] Han, B.Q., and Lavernia, E.J., "High-temperature behavior of a cryomilled ultrafine-grained Al-7.5% Mg alloy," *Materials Science and Engineering A* 410-411, 417-421 (2005).
- [46] Han, B.Q., Zhang, Z., and Lavernia, E.J., "Creep behaviour and thermal stability of cryomilled Al alloy," *Philosophical Magazine Letters* 85, no. 2, 97-108 (2005).
- [47] Montgomery, D.C. *Design and Analysis of Experiments*. John Wiley & Sons, New York (1997).
- [48] Ladani, L. and Nelson, S. "Transition of Crack Propagation Path Under Varied Levels of Load in Bimodal Grain Size Al-Mg Alloy" *J. Eng. Mater. Technol.* 133, 041017 (2011).
- [49] Dieter, G.F. *Mechanical Metallurgy*. McGraw-Hill, New York (1961).
- [50] *ASM Handbook Volume 12: Fractography*, American Society for Metals (1987).
- [51] Mesarovic, S.D. "Dynamic strain aging and plastic instabilities" *J.Mech.Phys.Solids* 43, no. 5, 671-700 (1995).
- [52] Harvey, E., Ladani, L., and Weaver, M., "Complete mechanical characterization of nanocrystalline Al-Mg alloy using nanoindentation," *Mechanics of Materials* 52, 1-11 (2012).

- [53] Fischer-Cripps, Anthony C., *Nanoindentation*, Springer Science+Business Media, LLC (2001).
- [54] Ramulu, M., Paul, G. and Patel, J. "EDM surface effects on the fatigue strength of a 15 vol% SiCp/Al metal matrix composite material," *Composite Structures* 54, no. 1, 79-86 (2001).
- [55] Rebelo, J.C., Dias, A.M., Kremer, D., and Lebrun, J.L. "Influence of EDM pulse energy on the surface integrity of martensitic steels." *Journal of Materials Processing Technology* 84, 90-96 (1998).
- [56] Hull, D. *Fractography: Observing, Measuring and Interpreting Fracture Surface Topography*. Cambridge University Press, Cambridge (1999).
- [57] Gottstein, G., *Physical Foundations of Materials Science*, Springer-Verlag, Berlin (2010).
- [58] Hu, T., University of California, Davis. Personal communication. (2012).
- [59] Han, B.Q., Lavernia, E.J., Mohamed, F.A., "Mechanical Behavior of a Cryomilled Near-Nanostructured Al-Mg-Sc Alloy," *Metallurgical and Materials Transactions A* 36A, 345-355 (2005).
- [60] Zhang, Z., Han, B.Q., Zhou, Y., and Lavernia, E.J., "Elevated temperature mechanical behavior of bulk nanostructured Al 5083-Al₈₅Ni₁₀La₅ composite," *Materials Science and Engineering A* 493, 221-225 (2008).
- [61] Joshi, S., Ramesh, K., Han, B. and Lavernia, E. "Modeling the constitutive response of bimodal metals" *Metallurgical and Materials Transactions A* 37, no. 8, 2397-2404 (2006).
- [62] Voce, E. "The Relationship between Stress and Strain for Homogeneous Deformation" *J Inst Met* 74, 537-562 (1948).
- [63] Peterson, D.R. Vishay Measurements Group, Inc. Personal communication. (2011).